

STATISTICS OF GRAVITATIONAL MICROLENSING MAGNIFICATION. II. THREE-DIMENSIONAL LENS DISTRIBUTION

MAN HOI LEE

Department of Physics, Queen's University, Kingston, ON K7L 3N6, Canada; mhlee@astro.queensu.ca

ARIF BABUL¹

Department of Physics, New York University, 4 Washington Place, New York, NY 10003; babul@almuhit.physics.nyu.edu

LEV KOFMAN

Institute for Astronomy, University of Hawaii, 2680 Woodlawn Drive, Honolulu, HI 96822; kofman@ifa.hawaii.edu

AND

NICK KAISER²

CIAR Cosmology Program, Canadian Institute for Theoretical Astrophysics, University of Toronto, 60 St. George Street, Toronto, ON M5S 1A7, Canada; kaiser@ifa.hawaii.edu

Received 1996 August 21; accepted 1997 June 24

ABSTRACT

In the first paper of this series, we studied the theory of gravitational microlensing for a planar distribution of point masses. In this second paper, we extend the analysis to a three-dimensional lens distribution. First we study the lensing properties of three-dimensional lens distributions by considering in detail the critical curves, the caustics, the illumination patterns, and the magnification cross sections $\sigma(A)$ of multiplane configurations with two, three, and four point masses. For N_* point masses that are widely separated in Lagrangian space (i.e., in projection), we find that there are $\sim 2^{N_*} - 1$ critical curves in total, but that only $\sim N_*$ of these produce prominent caustic-induced features in $\sigma(A)$ at moderate to high magnifications ($A \gtrsim 2$).

In the case of a random distribution of point masses at low optical depth, we show that the multiplane lens equation near a point mass can be reduced to the single-plane equation of a point mass perturbed by weak shear. This allows us to calculate the caustic-induced feature in the macroimage magnification distribution $P(A)$ as a weighted sum of the semianalytic feature derived in Paper I for a planar lens distribution. The resulting semianalytic caustic-induced feature is similar to the feature in the planar case, but it does not have any simple scaling properties, and it is shifted to higher magnification. The semianalytic distribution is compared with the results of previous numerical simulations for optical depth $\tau \approx 0.1$, and they are in better agreement than a similar comparison in the planar case. We explain this by estimating the fraction of caustics of individual lenses that merge with those of their neighbors. For $\tau = 0.1$, the fraction is $\approx 20\%$, much less than the $\approx 55\%$ for the planar case. In the three-dimensional case, a simple criterion for the low optical depth analysis to be valid is $\tau \ll 0.4$, though the comparison with numerical simulations indicates that the semianalytic distribution is a reasonable fit to $P(A)$ for τ up to 0.2.

Subject headings: gravitational lensing — methods: statistical

1. INTRODUCTION

The gravitational lensing effect of an ensemble of point masses has long been a subject of investigation (see Schneider, Ehlers, & Falco 1992 for a summary of earlier work; see also Kofman et al. 1997, hereafter Paper I, and references therein). Most studies have focused on the situation in which the spatial distribution of the point-mass lenses along the line of sight is “compact,” i.e., the size of the region within which the lenses are distributed is much smaller than the other distances (those between the source and the lenses and between the observer and the lenses) in the problem. For gravitational lensing calculations, a compact distribution of lenses is usually approximated by its projection onto a single lens plane. The important case of low optical depth, single-plane microlensing has been investigated in great detail (see Paper I and references therein), and we now understand reasonably well the caustic structure, the illumination pattern, the probability distribution

of macroimage magnification, and the flux variability of macroimages in this case.

There are, however, situations in which the lensing objects are modeled by an “extended” (or three-dimensional) distribution of point masses, i.e., by a point-mass distribution that is comparable in scale to the other distances in the problem. A well-known example is the microlensing of stars in the Large Magellanic Cloud and the Galactic bulge by foreground stars and, possibly, massive compact halo objects (MACHOs; Alcock et al. 1993, 1997; Aubourg et al. 1993; Udalski et al. 1993, 1994b; Ansari et al. 1996). The theoretical analysis of this problem is relatively simple, because the optical depth to microlensing is very small ($\tau < 10^{-5}$) and the point-mass lenses are essentially acting independently (Paczynski 1986, 1991; Griest 1991). (Note, however, that microlensing by physical binary systems is also possible; see Mao & Paczyński 1991; Udalski et al. 1994a; Alard, Mao, & Guibert 1995.) A more complicated problem is the possibility that a substantial fraction of the dark matter in the universe is in the form of compact objects (see, e.g., Carr 1994 and Dalcanton et al. 1994 for current limits). Then the universe as a whole has a

¹ Present address: Department of Physics and Astronomy, University of Victoria, P.O. Box 3055, Victoria, BC V8W 3P6, Canada.

² Present address: Institute for Astronomy, University of Hawaii, 2680 Woodlawn Drive, Honolulu, HI 96822.

significant optical depth to microlensing (Press & Gunn 1973). The theoretical aspects of this latter problem have been studied both analytically (e.g., Canizares 1982; Turner, Ostriker, & Gott 1984; Nemiroff 1989; Pei 1993) and through numerical simulations (Refsdal 1970; Schneider & Weiss 1988a, 1988b; Rauch 1991). The analytical studies have either completely ignored lensing by multiple lenses or used the approximation that the total magnification is the product of the magnifications due to the individual lenses. The multiplication approximation cannot be strictly justified, as it can fail greatly even for lens configurations in which all but one of the lenses can be treated as perturbations (see, e.g., Pei 1993; Schneider 1993). In the numerical studies (which fully accounted for lensing by multiple lenses), it was found that there are qualitative differences between two- and three-dimensional microlensing. For example, for $\tau \approx 0.1$, the three-dimensional macroimage magnification distribution does not show the prominent caustic-induced feature produced by a planar distribution of point masses (Rauch et al. 1992; but see § 4 below).

The usual approach to gravitational lensing by a three-dimensional distribution of lenses is the multiple lens plane approximation (Blandford & Narayan 1986; Kovner 1987). Compared with single-plane gravitational lensing, there have been few studies of multiplane gravitational lensing. This has perhaps been due to the lack of lensing candidates with lenses at different redshifts. However, recent observations of the lens systems 2345+007 (Pelló et al. 1996), 2016+112 (Lawrence, Neugebauer, & Matthews 1993), and 957+561 (Bernstein, Tyson, & Kochanek 1993; but see also Dahle, Maddox, & Lilje 1994) suggest that these systems may involve lenses at different redshifts. Besides the statistical microlensing studies mentioned above, there have been studies of statistical multiplane lensing by other types of lenses (Jaroszyński et al. 1990; Lee & Paczyński 1990; Babul & Lee 1991; Jaroszyński 1991; Wambsganss, Cen, & Ostriker 1996). There have also been studies of the basic mathematical properties of multiplane gravitational lensing (Levine & Petters 1993; Levine, Petters, & Wambsganss 1993; Petters 1995a, 1995b) and of the properties of some simple multiplane configurations (Kochanek & Apostolakis 1988; Erdl & Schneider 1993, hereafter ES; Petters & Wicklin 1995). Nevertheless, the properties of multiplane gravitational lensing and, in particular, the reasons for many of the differences between two- and three-dimensional microlensing are not yet well understood.

As we shall see in § 3, to understand some of the differences between two- and three-dimensional microlensing, it is useful to study in detail specific cases of simple three-dimensional lens configurations. The study by Erdl & Schneider (ES) of a lens system consisting of two point masses at different distances from the observer is a step in this direction. The study considered primarily the critical curves and the caustics and was able to obtain a complete classification of their topological properties with respect to the model parameters in this particular case.

The main goal of this study is to give a systematic theory of gravitational microlensing by a random distribution of point masses. In the accompanying Paper I, we refined the theory of gravitational microlensing for a planar distribution of point masses. In particular, we obtained a practical semianalytic expression for the macroimage magnification distribution, $P(A)$, for low optical depth τ , by allowing for the shear perturbations of neighboring lenses. In this paper,

we study the properties of gravitational microlensing by a three-dimensional distribution of point masses. We are interested in the critical curves, the caustics, the illumination pattern, and especially the macroimage magnification distribution. We shall not consider other interesting aspects such as time delays and the temporal behavior of microlensing events (note, however, that the latter is given by the magnification along tracks through the illumination pattern). In § 2, we present the lens equations. In § 3, we study in detail multiplane configurations with two, three, and four point masses to discover which new features are expected in three-dimensional microlensing. We also explain qualitatively why these new features arise. The case of low optical depth, three-dimensional microlensing is studied in § 4, using an approach similar to that used in Paper I to study the caustic-induced feature in $P(A)$ for a planar lens distribution. As in the planar case, low optical depth corresponds to the limit in which lensing by close groups of two (or more) point masses (in projection) is negligible. The resulting semianalytic $P(A)$ is compared with the numerical results of Rauch (1991), and the differences between the two- and three-dimensional results are discussed. Our conclusions are summarized in § 5.

2. LENS EQUATIONS

We begin by establishing the relevant equations for gravitational lensing by a three-dimensional lens distribution. As in Paper I, we shall only consider gravitational lensing in an Einstein-de Sitter cosmological background weakly perturbed by the gravitational field of the lenses. Our notation is identical to that used in Paper I, and the reader is referred to § 2 of Paper I for the definitions of terms not explicitly defined here.

Let us consider an isotropic point source at the origin of our coordinates and an observer plane at a comoving distance χ_{so} from the source (see Fig. 1). In the absence of perturbations, the observer plane would be uniformly illuminated, and a light ray that left the source with angle $\theta = (\theta_1, \theta_2)$ would pierce the observer plane at $x = \chi_{\text{so}}\theta$. This defines our planar Lagrangian coordinates x . In the presence of density inhomogeneities, the light ray would suffer deflections and pierce the observer plane at the Eulerian coordinates r .

For a three-dimensional (or extended) lens distribution, gravitational lensing is usually studied within the framework of the multiple lens plane approximation (Blandford & Narayan 1986; Kovner 1987). It is assumed that the lens distribution can be approximated by a series of N geometrically thin configurations, i.e., lens planes, and that the separations between the lens planes are sufficiently large. Then the deflection of a light ray by one of the lens planes is not influenced by the others, and a light ray is deflected N times on the way from the source to the observer (see Fig. 1). After $j-1$ deflections, the location at which the light ray pierces the j th lens plane, projected onto the observer plane, is

$$x_j = x_1 + \sum_{i=1}^{j-1} \beta_{ij} s_i(x_i), \quad (1)$$

where $s_i(x_i)$ is the deflection by the i th plane (which can be expressed as the gradient with respect to x_i of an effective surface gravitational potential on plane i), β_{ij} is a dimen-

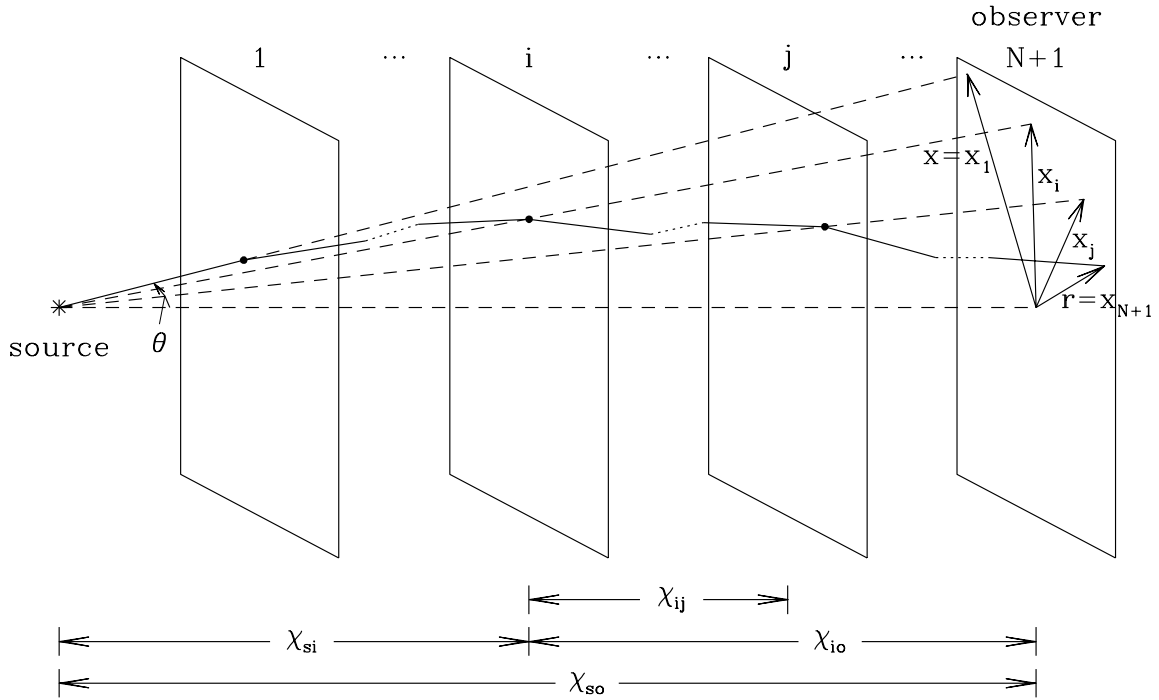


FIG. 1.—Schematic diagram illustrating our notation for multiplane gravitational lensing. A light ray that leaves the source with angle θ has Lagrangian coordinates $x (=x_1 = \chi_{so} \theta)$. It is deflected on the N lens planes and reaches the observer plane at Eulerian coordinates $r (=x_{N+1})$.

sionless distance parameter defined by

$$\beta_{ij} \equiv \frac{\chi_{ij} \chi_{so}}{\chi_{sj} \chi_{io}}, \quad (2)$$

and χ_{ij} is the comoving distance between planes i and j . Note that β_{ij} can take on values between 0 (in the limit $i = j$) and 1 (in the limit $i = \text{"s"}$ or $j = \text{"o"}$). If we denote the observer plane as plane $N + 1$, then the Lagrangian-to-Eulerian mapping is

$$r = x + s, \quad (3a)$$

where

$$r = x_{N+1}, \quad x = x_1, \quad s = \sum_{i=1}^N s_i(x_i). \quad (3b)$$

Unlike the single-plane lens mapping, this multiplane lens mapping is not, in general, a gradient mapping. For the particular case in which the lens planes are populated by point masses,

$$s_i(x_i) = -4G \left(\frac{\chi_{io} \chi_{so}}{a_i \chi_{si}} \right) \sum_k m_{ik} \frac{x_i - x_{ik}}{|x_i - x_{ik}|^2}, \quad (4)$$

where a_i is the cosmological scale factor at the redshift of lens plane i and x_{ik} is the location of the k th lens (of mass m_{ik}) on lens plane i . Note that x_{ik} is the position projected onto the observer plane, i.e., $x_{ik} = \chi_{so} \theta_{ik}$, where θ_{ik} is the angular position of the lens from the source. Hereafter, we shall assume for the sake of simplicity that all the point masses have the same mass m . Then

$$s_i(x_i) = -x_{E,i}^2 \sum_k \frac{x_i - x_{ik}}{|x_i - x_{ik}|^2}, \quad (5)$$

where

$$x_{E,i} \equiv \left(\frac{4Gm\chi_{io}\chi_{so}}{a_i\chi_{si}} \right)^{1/2} \quad (6)$$

is the (Lagrangian) Einstein radius of a point mass on the i th lens plane. For a random distribution of point masses, the optical depth to microlensing is $\tau = \pi \sum_{i=1}^N n_i x_{E,i}^2$, where $n_i = (a_i \chi_{si}/\chi_{so})^2 \Sigma_i/m$ and Σ_i are, respectively, the projected (onto the observer plane) surface number density and the physical surface mass density of point masses on lens plane i . When we consider the situation in which a significant fraction of the dark matter in the universe is in the form of cosmologically distributed compact objects, since the mean of the density inhomogeneities should be zero, we should compensate the randomly distributed point masses on each plane by a *negative* smooth surface mass density. Then a term of the form $\pi n_i x_{E,i}^2 x_i$ should be added to the right-hand side of equation (5).

3. MULTIPLANE LENSING BY A FEW POINT MASSES

As we mentioned in § 1, numerical simulations of gravitational microlensing by a three-dimensional random distribution of point masses have revealed differences between two- and three-dimensional microlensing (Refsdal 1970; Schneider & Weiss 1988a, 1988b; Rauch 1991). To determine and understand qualitatively some of these differences, it is useful to study in detail specific cases of simple lens configurations. In this section, we study numerically the properties of multiplane gravitational lensing by a few point masses. To reduce the number of parameters, we restrict our study to cases in which the distance between the source and the observer is much smaller than the horizon scale, i.e., $a_s \approx a_0$ or source redshift $z_s \ll 1$.

If there are N_i point masses on lens plane i (we shall denote the total number of point masses as $N_* = \sum_{i=1}^N N_i$),

the sum of the squared (Lagrangian) Einstein radii is

$$x_E^2 \equiv \sum_{i=1}^N N_i x_{E,i}^2. \quad (7)$$

For the numerical computations, it is convenient to express all positions in units of x_E and to define a dimensionless mass parameter

$$m'_i \equiv x_{E,i}^2/x_E^2, \quad (8)$$

so that $\sum_{i=1}^N N_i m'_i = 1$. Then the multiplane lens equation with identical point masses (eqs. [1], [5]) can be written as

$$\mathbf{x}_j = \mathbf{x}_1 - \sum_{i=1}^{j-1} \beta_{ij} m'_i \sum_k \frac{\mathbf{x}_i - \mathbf{x}_{ik}}{|\mathbf{x}_i - \mathbf{x}_{ik}|^2}. \quad (9)$$

3.1. Configurations with Two Point Masses

First, let us consider in detail configurations with two point masses. Without any loss of generality, we can choose a coordinate system such that $\mathbf{x}_{11} = 0$ and $\mathbf{x}_{21} = (d, 0)$. Since we assume that $a_s \approx a_0$, the two remaining parameters, β_{12} and m'_1 , are related by $m'_1 = 1/(2 - \beta_{12})$.

The topology of the critical curves (and the caustics) as a function of the parameters (d, β_{12}, m'_1) has been classified by ES (see also Schneider & Weiss 1986 for the $\beta_{12} = 0$ case). In general, for given β_{12} and m'_1 , there are five transitions in the topology of the critical curves as d increases from zero (see Fig. 6 of ES). However, in the limit $\beta_{12} \rightarrow 0$ (i.e., in the limit of two point masses on the same plane), three of the transitions merge at $d = 0$, and the number of transitions is reduced to two. For comparison, we show in Figures 2–7 two sets of models with $\beta_{12} = 0$ and $\beta_{12} = 0.3$. (We have also computed models with $\beta_{12} = 0.6$, but the results are qualitatively similar to those with $\beta_{12} = 0.3$ and are not shown here.) The configurations shown in Figures 2–7 were chosen to sample regions of the parameter space with different critical curve topologies. The parameters (β_{12}, d) and the critical curve topology types (in the notation of ES) of these configurations are listed in Table 1. [Note that the topology type F is not represented; with $m'_1 = 1/(2 - \beta_{12})$, type F only occurs at very small d .]

In Figures 2 and 5, we show the critical curves and the caustics of the configurations with $\beta_{12} = 0$ and 0.3, respectively. The corresponding magnification patterns (and some isomagnification contours) on the observer plane are shown in Figures 3 and 6. In Figures 4 and 7, we plot the “normalized” differential cross section $\varphi(A) \equiv \sigma(A)/\sigma_0(A)$, where $\sigma(A)$ is the differential cross section for magnification A and

$$\sigma_0(A) = \frac{2\pi x_E^2}{(A^2 - 1)^{3/2}} \quad (10)$$

is the differential cross section of a single, isolated point-mass lens with Einstein radius x_E , as defined in equation (7). As we saw in Paper I (see also § 4 below), the function $\varphi(A)$ is a useful measure of the deviations of the cross section of a more complex lens configuration from that of the point-mass lens. The cross sections and the magnification patterns shown in these (and all subsequent) figures were obtained by using the ray-shooting method (see, e.g., Kayser, Refsdal, & Stabell 1986; Schneider & Weiss 1986, 1988b). Since the magnification factor is calculated in this method by collecting rays into a grid of square pixels, it is the magnification for an observing device (or, equivalently, a source) of the

TABLE 1
CONFIGURATIONS WITH TWO POINT
MASSES

d	Topology	Pixel Sizes
$\beta_{12} = 0.0$:		
2.4.....	A'	0.020, 0.032
1.0.....	B'	0.016, 0.024
0.6.....	C'	0.016, 0.024
$\beta_{12} = 0.3$:		
2.0.....	A	0.020, 0.040
1.0.....	B	0.018, 0.036
0.6.....	C	0.016, 0.032
0.5.....	D	0.016, 0.032
0.4.....	E	0.016, 0.032
0.2.....	E	0.020, 0.040

size of 1 pixel. To assess the effects of finite pixel size, we performed two sets of calculations, with the linear pixel sizes in one set smaller by a factor of 1.5–2 (see Table 1). The smaller pixels (which correspond to a 500^2 pixel grid that must cover at least all of the isomagnification contours significantly affected by the caustics) resolve all (except the very small) caustics. We show in Figures 3 and 6 the magnification patterns from the calculations with the smaller pixels and, in Figures 4 and 7, the function $\varphi(A)$ from both sets of calculations. By comparing the two sets of $\varphi(A)$ and examining the magnification patterns, we find that the function $\varphi(A)$ from the calculations with the smaller pixels is (not) significantly affected by the finite pixel size at A larger (smaller) than that marked by the dotted lines in Figures 4 and 7. As expected (Rauch et al. 1992), the finite pixel size introduces an upper limit to the magnification factor and produces extra “bumps” in $\varphi(A)$ (at A larger than that marked by the dotted lines). The real caustic-induced features in $\varphi(A)$ are at A smaller than that marked by the dotted lines, and they are not significantly affected by the finite pixel size.

The $\beta_{12} = 0$ (and $m'_1 = 0.5$) models have already been studied in detail by Schneider & Weiss (1986); hence, we only give a brief description of these models here. For $d \gg 2$, the region near each of the point masses is perturbed by the weak shear from the other point mass. So we have two critical lines that are slightly flattened ellipses and two caustics that have the familiar “astroid” shape (see § 3 and Fig. 2 of Paper I). As $d \rightarrow 2$, the critical curves and the caustics become asymmetric (Fig. 2a). The corresponding differential cross section (Fig. 4a) shows caustic-induced features that are similar to those found in the case of a point mass perturbed by shear (see Fig. 3 of Paper I). There is, in addition, a bump (at $A \approx 2$) that is associated with the last isomagnification contour that encloses both caustics (see Fig. 3a). As d decreases below 2, the number of critical curves (and caustics) changes from two to one and, finally, to three, and the topology of the critical curves (and the caustics) changes from A' to B' to, finally, C' (see Table 1). In all cases, there are caustic-induced features in the differential cross section at moderate to high A ($\gtrsim 1.5$), and the cross section at small A ($A - 1 \sim 0.1$) is reduced. Each of these features is associated with either a local minimum, or saddle point, in the magnification pattern or an isomagnification contour that touches the caustics at one or more points. In the latter case, the contours of slightly larger A are broken into disconnected, shorter segments by the caustics, and the loss of the area inside the caustics results in a drop in $\varphi(A)$. (An example that has been dis-

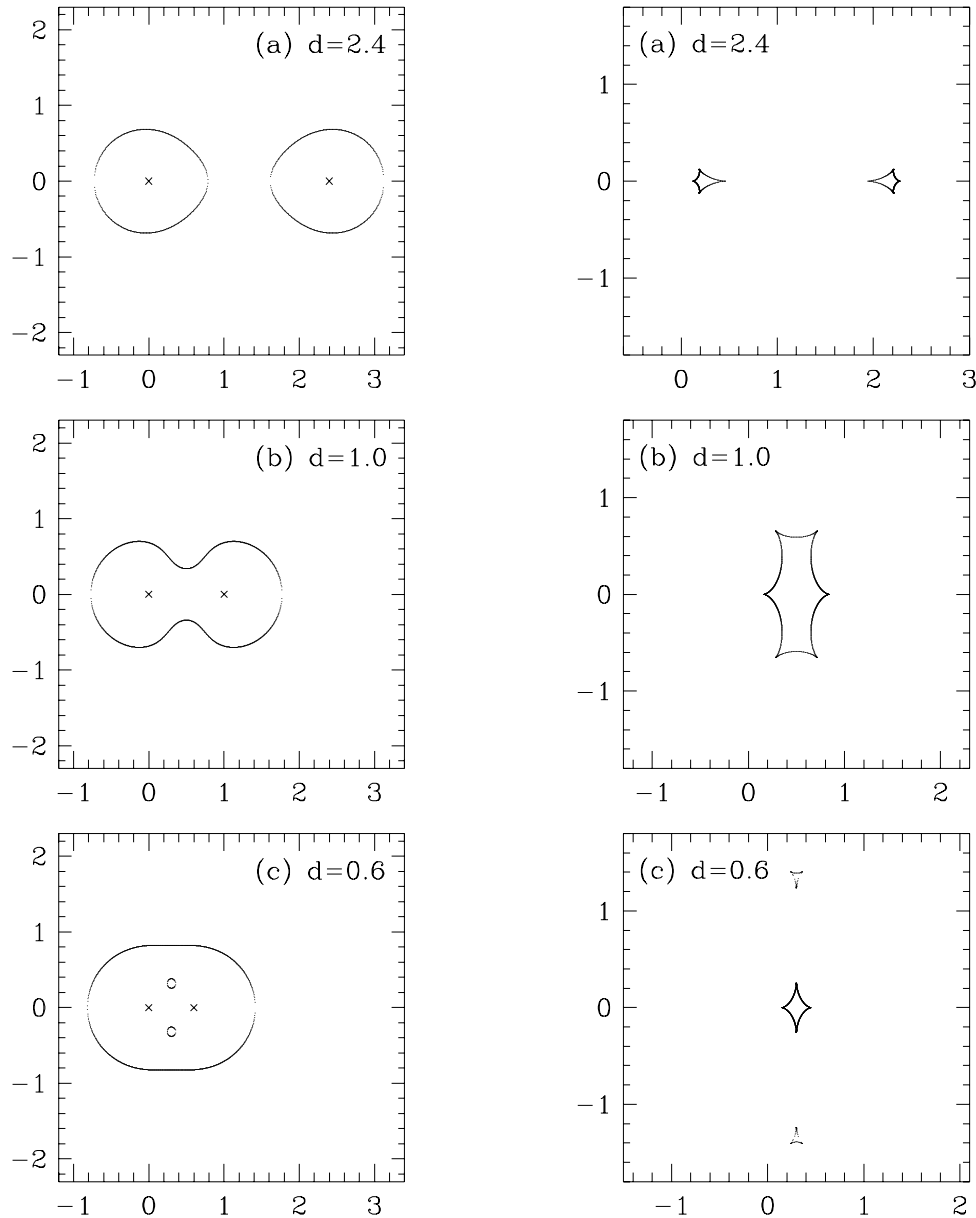


FIG. 2.—Critical curves (*left*) and caustics (*right*) of the configurations with two point masses [$m'_1 = 1 - m'_2 = 1/(2 - \beta_{12})$]. The dimensionless distance between the lens planes $\beta_{12} = 0$ (i.e., the two point masses are on the same plane). Each panel is labeled by the Lagrangian separation, d , between the two point masses, whose Lagrangian positions are indicated by the crosses.

cussed in detail in § 3 of Paper I is the feature associated with the contour osculating the astroid-shaped caustic of the point-mass plus weak-shear lens.)

When the two point masses are not on the same lens plane, there are new features and transitions in the critical curves and the caustics (see Fig. 5). At large Lagrangian separation d (Fig. 5a), besides the two critical curves that are similar to those seen in the $\beta_{12} = 0$ case (see § 4 for an explanation), there is an extra critical curve inside the critical curve that encloses point mass 1 (i.e., the point mass closer to the source). This critical curve is offset from point mass 1 in the direction opposite point mass 2, and both its size and its distance from point mass 1 increase as d decreases. The corresponding caustic is located at a large distance along the positive x -axis. This caustic has the (asymmetric) astroid shape of the two caustics that are known from the $\beta_{12} = 0$ case, and it increases in size and

moves toward the other two caustics as d decreases. The critical curve (and caustic) configuration at large d that we have just described is denoted as topology type A by ES. Except for the presence of the new critical curve and caustic, the topological transitions shown in Figures 5a–5c are similar to those shown in Figure 2. The remaining transitions do not exist in the single lens plane case. However, as ES pointed out, except for the elliptic umbilic transition between C and D, all transitions are of the beak-to-beak type.

We can explain the new critical line (and caustic) and its qualitative behavior if we focus on the configurations of topology types A–C. For these configurations, it is clear that the new critical line is composed of the set of rays that are strongly deflected by point mass 1 (on lens plane 1) to the vicinity of point mass 2 (on lens plane 2) and are then infinitely magnified by point mass 2. Obviously, this process

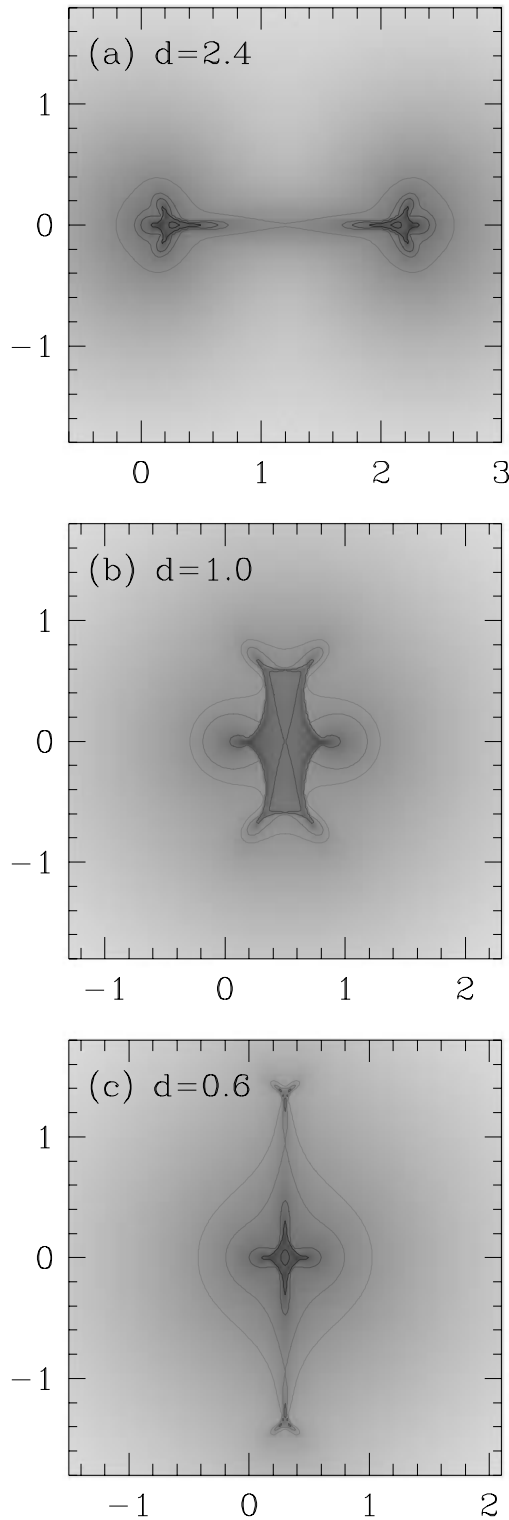


FIG. 3.—Magnification patterns and isomagnification contours of the configurations shown in Fig. 2. The gray scale is linear in $\log(A - 1)$ (with the higher magnification area darker), and the contour levels are chosen to highlight interesting features in the magnification patterns.

can only occur when the point masses are not on the same lens plane. The new critical line is closer to point mass 1 for larger d , because a light ray must be more strongly deflected by point mass 1 to reach the vicinity of point mass 2.

In the magnification patterns (Fig. 6), there are local minima and saddle points that are associated with the new

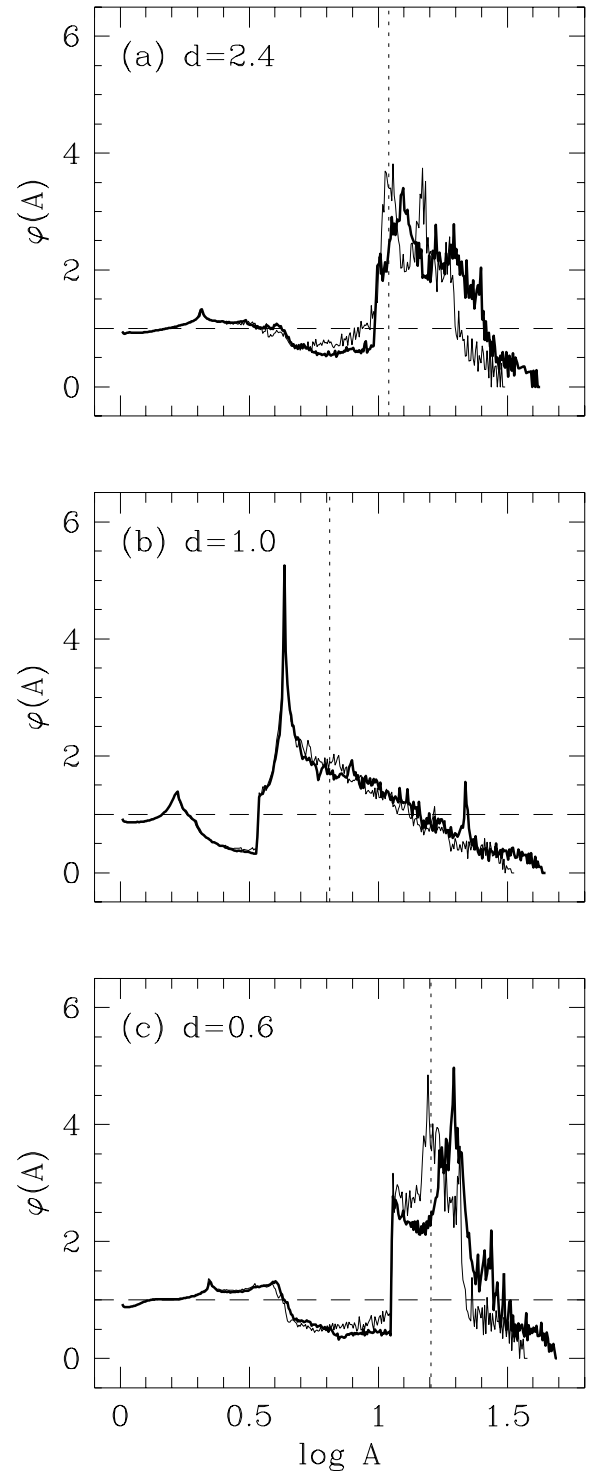


FIG. 4.—“Normalized” differential cross sections, $\phi(A)$, of the configurations shown in Fig. 3. Note that $\phi(A) = 1$ for a single point mass of unit mass. In each panel, the thick (thin) line was obtained from the ray-shooting calculation with the smaller (larger) pixel size listed in Table 1. The small pixel results (thick lines) are not significantly affected by the finite pixel size at A smaller than that marked by the dotted lines.

caustic; there are also isomagnification contours that touch the new caustic at two points (e.g., the outermost contour in Fig. 6d). These new features in the magnification patterns are expected to produce corresponding features in the cross sections. However, as we can see in Figure 7, the “normalized” differential cross sections $\phi(A)$ are actually

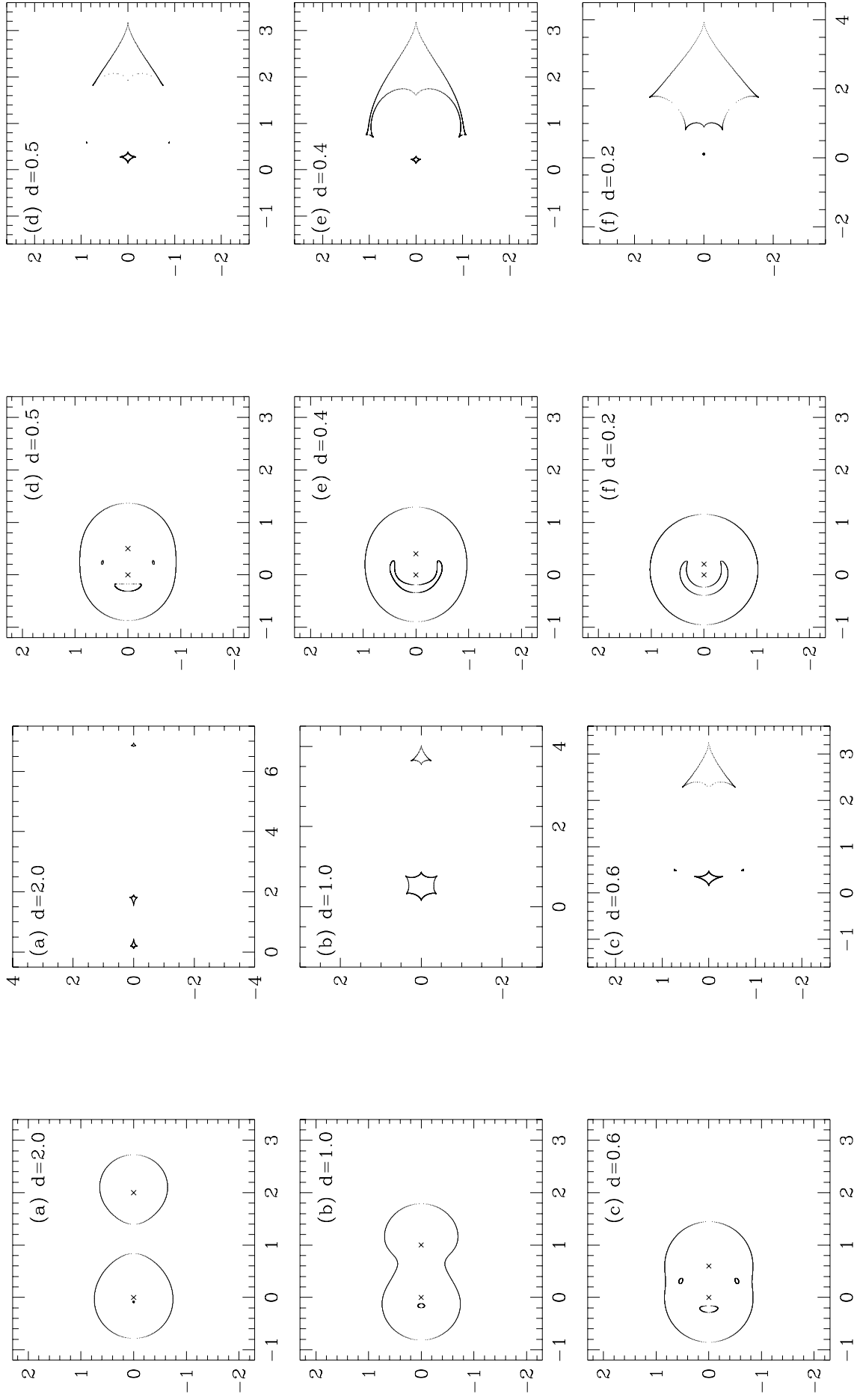


FIG. 5.—Same as Fig. 2, but for the configurations with $\beta_{12} = 0.3$

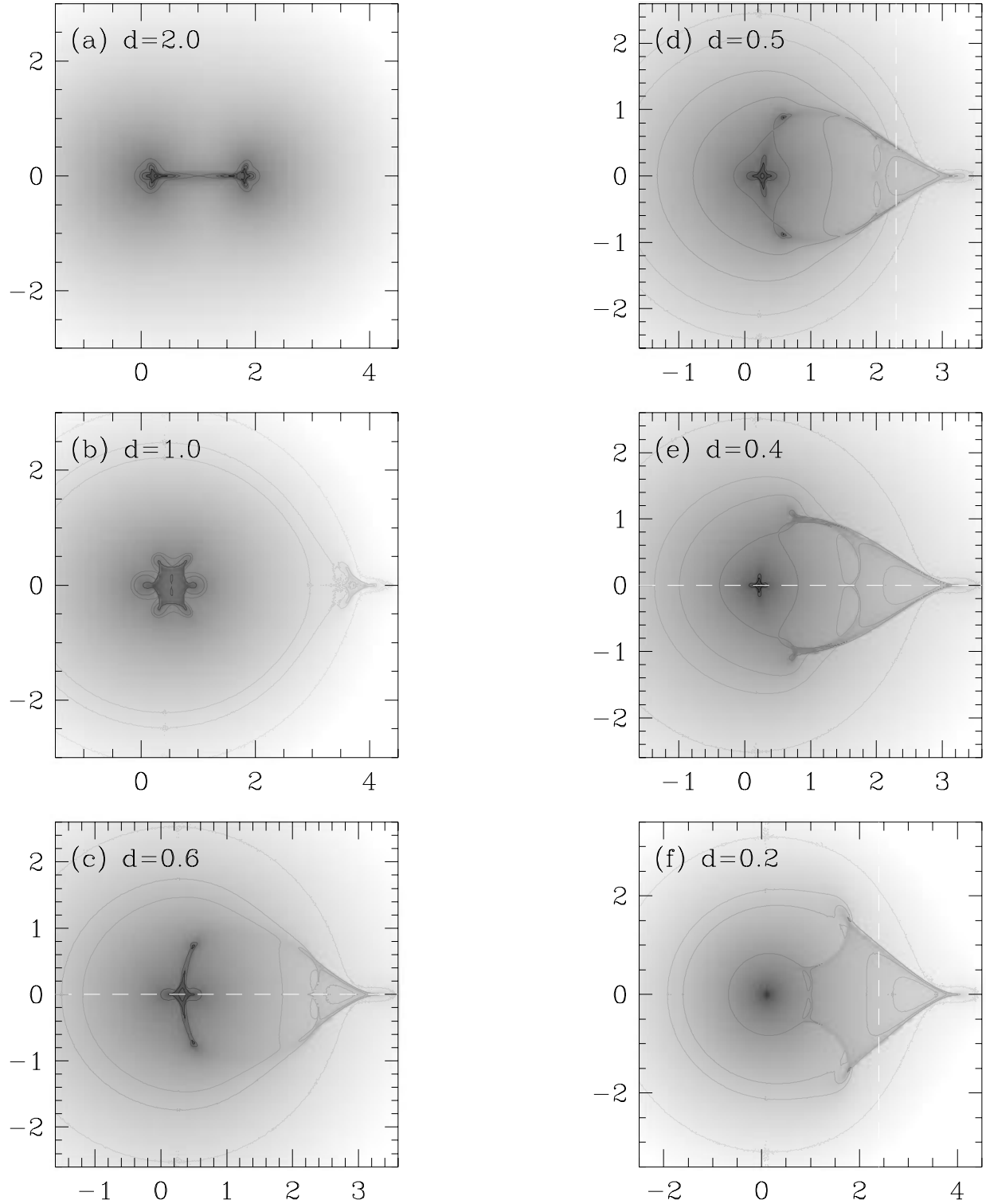


FIG. 6.—Same as Fig. 3, but for the configurations shown in Fig. 5. The magnification profiles along the dashed lines are shown in Fig. 8.

quite similar to those shown in Figure 4. Features associated with the new caustic are not noticeable until $d \lesssim 0.6$, and even in cases in which the new caustic (which is transformed at small d) encloses a large area of the observer plane, the new features are typically weak and at $A \lesssim 2$. (They are stronger and at higher A for the $\beta_{12} = 0.6$ models.)

If we examine the magnification patterns (and Fig. 8)

more carefully, we see that the new caustic is usually located in regions where the background magnification is small ($A \lesssim 2$). In addition, the magnification throughout most of the region inside the new caustic and, in particular, the minimum magnification inside the new caustic are only slightly higher than the low background magnification. Hence the new features in the magnification patterns and the corresponding features in $\varphi(A)$ have $A \lesssim 2$. Next let us

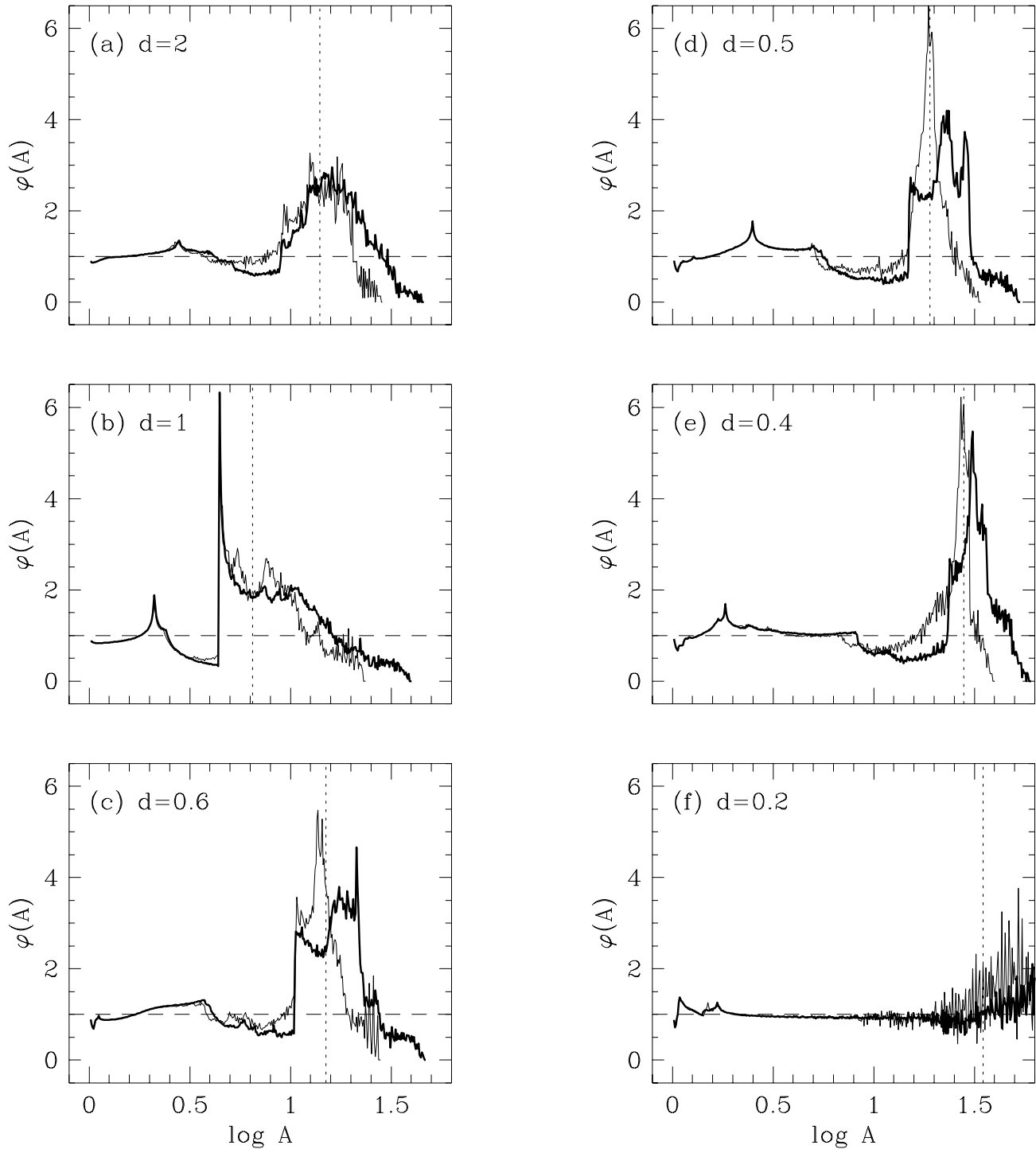


FIG. 7.—Same as Fig. 4, but for the configurations shown in Fig. 6

consider specifically the feature associated with the iso-magnification contour that touches the new caustic at two points (e.g., the outermost contour in Fig. 6*d*). This contour is long and, except for the distortion near the new caustic, nearly circular. Contours of slightly higher magnification are broken by the new caustic into a short arc around one of the cusps and a long arc that encloses the other caustic(s). This results in a decrease in the cross section $\sigma(A)$, because an area that would otherwise be enclosed by two of these contours (of magnification A and $A + dA$) is lost to the

interior of the caustic. Although the area lost to the caustic can be large, it is typically much smaller than the area enclosed by the long (and the short) arcs. Consequently, the decrease in $\phi(A) = \sigma(A)/\sigma_0(A)$, which is approximately the fractional decrease in $\sigma(A)$, is small. Similarly, the increase in $\phi(A)$ at $A = A_{\min}$, where A_{\min} is the minimum magnification inside the new caustic, is small because A_{\min} is typically small and the area enclosed by the contours of magnification A_{\min} and $A_{\min} + dA$ outside the new caustic (mainly two long arcs) is much larger than the area enclosed

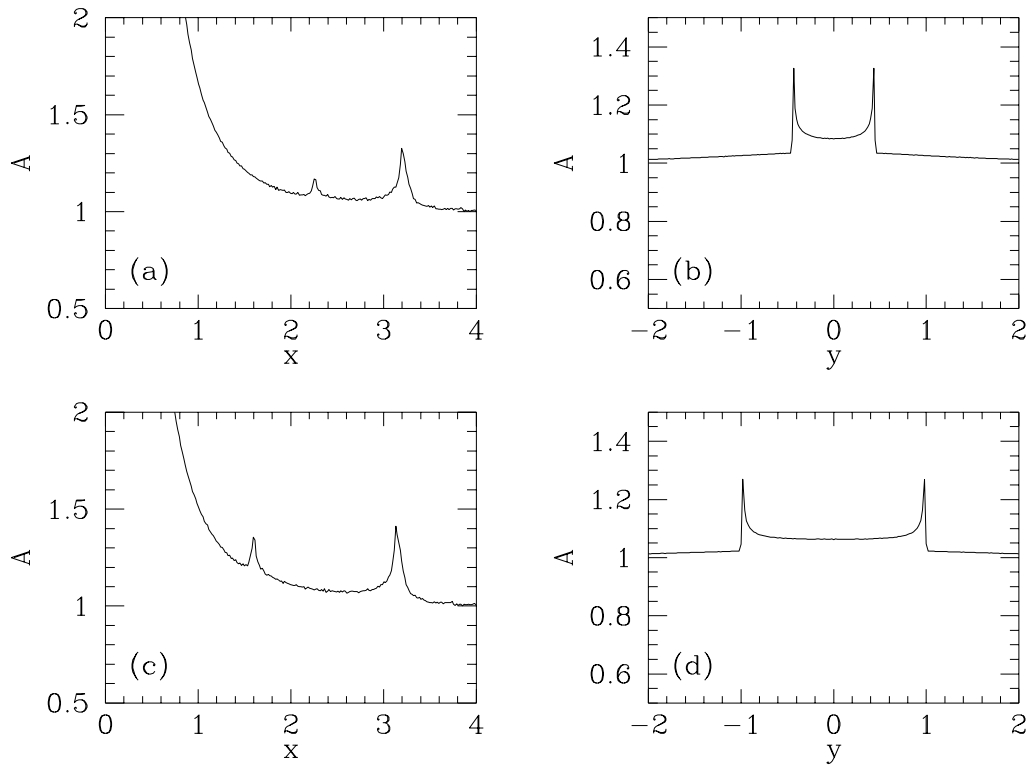


FIG. 8.—(a) Magnification factor A as a function of the x -coordinate for the magnification pattern shown in Fig. 6c and $y = 0$. (b) Magnification factor A as a function of the y -coordinate for the magnification pattern shown in Fig. 6d and $x = 2.3$. (c) Same as (a), but for Fig. 6e. (d) Same as (b), but for Fig. 6f and $x = 2.4$.

by the contour $A_{\min} + dA$ inside the new caustic.

The relatively weak influence of the new caustic on the magnification pattern is demonstrated more clearly in the sample of magnification profiles plotted in Figure 8. Although the magnification must be infinite on the caustic, only a very small region near the caustic has $A \gg 1$. In fact, the numerically obtained A , which is finite at a caustic because of the finite pixel size of our calculations, shows a maximum at the new caustic that is quite small ($\lesssim 2$). This behavior of the magnification pattern near the new caustic matches the description of the “thin caustics” found in the microlensing simulations of Schneider & Weiss (1988b). We have therefore found in the simple two-point-mass case a clear demonstration of the occurrence of thin caustics. As we mentioned earlier, the new caustic consists of light rays that are strongly deflected by the first point mass to the vicinity of the second point mass and are then infinitely magnified by the second point mass. In the simulations of Schneider & Weiss, which have a large number of point masses distributed on several lens planes, a light ray can be strongly deflected on more than one lens plane. It is likely that most of the caustics that are strongly deflected on one or more lens planes (i.e., the secondary caustics defined in § 3.2 below) are thin caustics. This identification for the thin caustics is consistent with the conjecture by Schneider & Weiss that the thin caustics are caused by steep deflection gradients, because the regions (in Lagrangian space) with strong deflections are also regions with steep deflection gradients.

3.2. Configurations with Three and Four Point Masses

Now let us consider briefly configurations with three and four point masses. Two configurations with $N_* = 3$ point

masses and one with $N_* = 4$ are shown in Figures 9, 10, and 11. These configurations have one point mass on each lens plane (i.e., $N = N_*$), and their parameters are listed in Table 2. The configuration *a* with $N_* = 3$ was chosen because it has the critical curve topology of point masses widely separated in Lagrangian space (i.e., in projection) while the smaller critical curves are clearly resolved. The other configurations are “typical” configurations resulting from randomly distributing the point masses within a cone of constant Lagrangian radius. We have (arbitrarily) chosen a cone radius such that a light ray passing within the cone would be infinitely magnified if the mass of the lenses were uniformly distributed within the cone.

A striking feature of Figure 9 (and Fig. 5) is the rapid increase in the number of critical curves with N_* . For a configuration with N_* point masses well separated in Lagrangian space and with each point mass on its own lens

TABLE 2
CONFIGURATIONS WITH THREE AND FOUR POINT MASSES

i	χ_{sil}/χ_{so}	x_{i1}	Pixel Sizes
Case a , $N_{*} = 3$:			
1	0.1	(−0.50, 0.00)	0.010, 0.024
2	0.5	(0.20, 0.00)	
3	0.9	(0.30, 0.25)	
Case b , $N_{*} = 3$:			
1	0.55032	(0.35, 0.00)	0.012, 0.024
2	0.79370	(−0.40, 0.65)	
3	0.94104	(−0.30, −0.50)	
Case c , $N_{*} = 4$:			
1	0.5	(0.30, 0.00)	0.012, 0.024
2	0.72112	(0.00, 0.65)	
3	0.85499	(−0.80, 0.00)	
4	0.95647	(0.00, −0.50)	

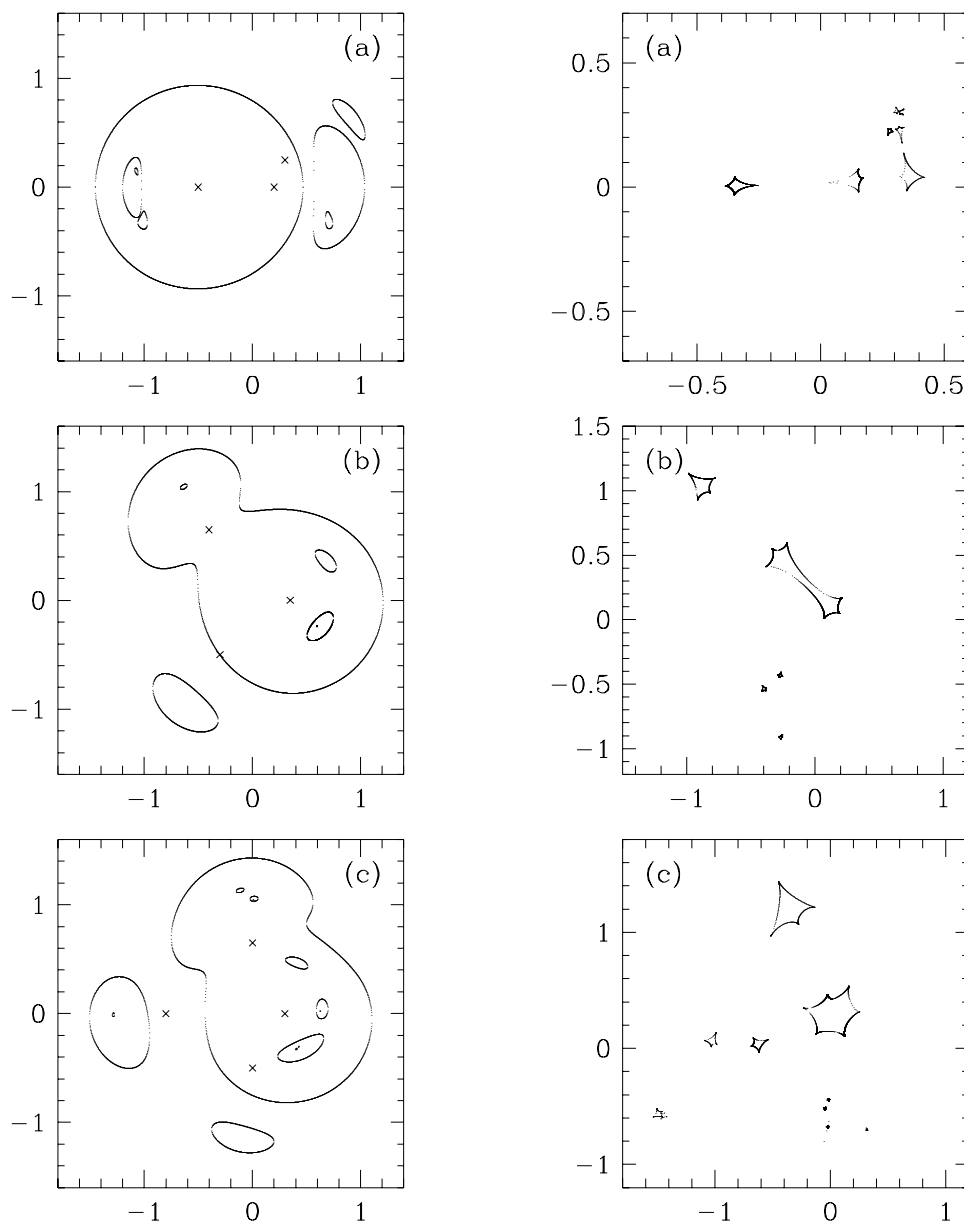


FIG. 9.—(a–c) Critical curves (left) and caustics (right) of configurations *a*, *b*, and *c* of Table 2, respectively. The Lagrangian positions of the point masses are indicated by the crosses.

plane (i.e., $N = N_*$), we can calculate the number of critical curves by extending the discussion given in § 3.1 for the origin of the new critical curve. Light rays from the source can reach the vicinity of the point mass on the i th lens plane after being strongly deflected by any combination (or none) of the previous $i - 1$ point masses. For each combination, there is a set of rays that are infinitely magnified by the i th point mass (and the weak deflections on the remaining planes). Therefore, there are 2^{i-1} critical curves associated with the i th point mass, and the total number of critical curves is $2^{N_*} - 1$. The critical curves shown in Figures 5a and 9a are consistent with these numbers. (The total number of critical curves is smaller for configurations with $N < N_*$ and approaches N_* in the limit $N = 1$, i.e., in the single lens plane case.) Hereafter, we shall refer to the caustics that are not strongly deflected as the *primary* caustics and those that are strongly deflected on at least one lens plane as the *secondary* caustics.

Although the number of critical curves increases exponentially with N_* , we can see in Figure 9 that the size of a critical curve decreases rapidly as the number of strong deflections associated with the critical curve (or, equivalently, the number of critical curves within which it is nested) increases. On the other hand, as in the two-point-mass case, a caustic formed after a larger number of strong deflections is not necessarily smaller. For example, in Figure 9c, the caustic located near $(-0.3, 1.2)$ [which corresponds to the critical curve located near $(0.25, -0.4)$] and the caustic with six cusps (which corresponds to the largest critical curve) are comparable in size.

In the two-point-mass case, because of the absence of overlapping or self-intersecting caustics, a complete classification of the critical curve topology also provides a complete classification of the caustic topology (ES). This is not true when $N_* > 2$. In particular, there are overlaps of caustics that belong to different critical curves. Examples of such

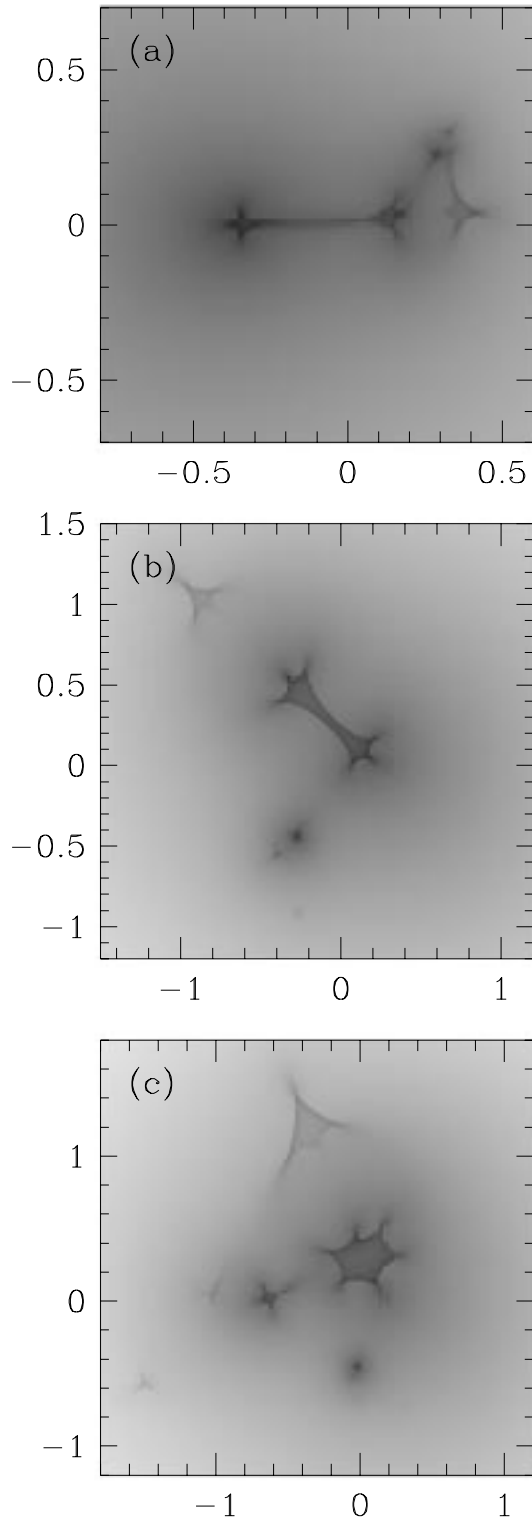


FIG. 10.—Magnification patterns of the configurations shown in Fig. 9. The gray scale is linear in $\log(A - 1)$ (with the higher magnification area darker).

overlapping caustics are the caustics located near (0.3, 0.3) in Figure 9a and those in the lower left corner of Figure 9c. (There are no self-intersecting caustics in the configurations shown in Fig. 9, but they may be present in other configurations.)

Finally, we discuss the normalized differential cross sections plotted in Figure 11. For the “typical” configurations

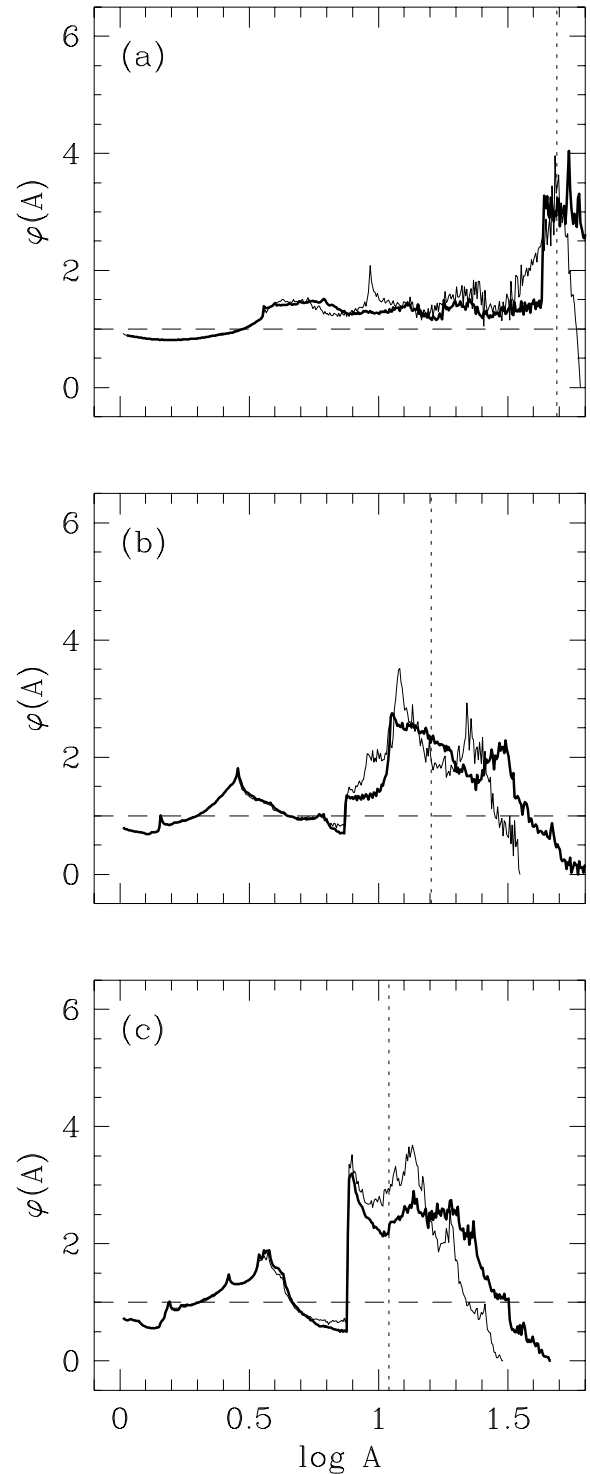


FIG. 11.—“Normalized” differential cross sections, $\phi(A)$, of the configurations shown in Fig. 10. In each panel, the thick (thin) line was obtained from the ray-shooting calculation with the smaller (larger) pixel size listed in Table 2. The small pixel results (thick lines) are not significantly affected by the finite pixel size at A smaller than that marked by the dotted lines.

b and *c*, the qualitative behaviors of $\phi(A)$ agree with what one might expect from the two-point-mass configurations studied in § 3.1. The cross section at small A ($A - 1 \sim 0.1$) is smaller than that for a single point mass. There are prominent features at moderate to high A ($\gtrsim 2$) that are associated

with the primary caustics. Features associated with the secondary caustics are typically weak, but some are noticeable at $A \lesssim 2$. For configuration a , the features associated with the primary caustics, i.e., those at $\log A \gtrsim 0.8$, are similar to the features in Figures 4a and 7a. This is expected since configuration a has the critical curve topology of widely separated point masses. However, the features associated with the secondary caustics are at unusually high A : the “plateau” between $\log A \approx 0.55$ and $\log A \approx 0.8$ consists of a series of such features. This is a result of the fact that the parameters of configuration a were specially chosen so that the smaller critical curves were clearly resolved. For these parameters, the caustics are unusually close to one another (see Fig. 9a, and note the change in scale between Figs. 9a and 9b). As a result, the secondary caustics are located in regions of relatively high background magnification (see Fig. 10a), and the associated features in $\varphi(A)$ are at unusually high A .

4. THREE-DIMENSIONAL, LOW OPTICAL DEPTH MICROLENSING

The study of simple lens configurations in the previous section shows that microlensing by a three-dimensional distribution of point masses is, in general, much more complicated than microlensing by lenses confined to a single lens plane. But there are also indications that, in the low optical depth limit, some aspects of the three-dimensional problem can be reduced to the planar one. For example, the multi-plane configurations with point masses widely separated in Lagrangian space (i.e., in projection) show primary caustics and corresponding features in $\varphi(A)$ that are similar to those found in the single-plane configurations. In § 4.1, we confirm this analytically for the limiting case of a point-mass lens perturbed by the weak shear from the other lenses. Another useful result from § 3 is that the significant features in $\varphi(A)$ at $A \gtrsim 2$ are associated with the primary caustics. Therefore we can neglect the features associated with the secondary caustics when we analyze the macro-image magnification distribution, $P(A)$, at $A \gtrsim 2$. In § 4.2, we derive the feature induced by the primary caustics at the high-magnification ($A \sim 1/\tau$) end of $P(A)$ for a three-dimensional, low optical depth lens distribution. The resulting semianalytic $P(A)$ is compared with previous numerical results in § 4.3, and the differences between the two- and three-dimensional results are discussed in § 4.4.

4.1. Cross Section of the Point-Mass Lens Plus Weak Shear in Three Dimensions

In the low optical depth limit, lensing (other than low-magnification events) by a three-dimensional distribution of point masses is, as in the planar case, typically dominated by a single point mass. Without loss of generality, we shall designate one of the point masses residing on the L th lens plane as dominant and locate this point mass at the origin of the lens screen. On all the other screens, the light ray is only weakly perturbed, and the perturbations are expanded to the first order in x_i . Before the light ray passes the L th screen with the dominant lens (i.e., for $j \leq L$), the lens mapping (eqs. [1], [5]) is simplified to

$$x_j = x_1 + \sum_{i=1}^{j-1} \beta_{ij}(\alpha_i + \hat{S}_i x_i), \quad (11)$$

where the constant deflection

$$\alpha_i = x_{E,i}^2 \sum_k \frac{x_{ik}}{|x_{ik}|^2} \quad (12a)$$

and the shear matrix

$$\hat{S}_i = x_{E,i}^2 \sum_k \frac{1}{|x_{ik}|^4} \begin{pmatrix} x_{ik}^2 - y_{ik}^2 & 2x_{ik}y_{ik} \\ 2x_{ik}y_{ik} & y_{ik}^2 - x_{ik}^2 \end{pmatrix} \quad (12b)$$

(similar to α_L and \hat{S}_L defined in eq. [13] of Paper I) represent the perturbative influence of the lenses on the i th plane. Equation (11) can also be written as

$$x_j = \hat{B}_j x_1 + u_j, \quad (13)$$

where

$$\hat{B}_j = \hat{I} + \sum_{i=1}^{j-1} \beta_{ij} \hat{S}_i \hat{B}_i, \quad u_j = \sum_{i=1}^{j-1} \beta_{ij}(\alpha_i + \hat{S}_i u_i), \quad (14)$$

and \hat{I} is the identity matrix. Once the light ray has traversed the L th lens screen, the location at which the light ray intersects subsequent (i.e., $j > L$) screens is given by

$$x_j = \hat{B}_j x_1 + u_j + \beta_{Lj} \hat{C}_j d_L(x_L), \quad (15)$$

where

$$d_L(x_L) = -x_{E,L}^2 \frac{x_L}{|x_L|^2} \quad (16)$$

denotes the influence of the dominant lens and

$$\hat{C}_j = \hat{I} + \sum_{i=L+1}^{j-1} \left(\frac{\beta_{ij} \beta_{Li}}{\beta_{Lj}} \right) \hat{S}_i \hat{C}_i. \quad (17)$$

Note that, in the absence of the dominant lens, u_j is the path followed by a light ray with $x_1 = 0$.

On the observer plane [which is the $(N+1)$ th screen, but we also denote it with the subscript “o”], the Eulerian position is given by

$$r = \hat{B}_o x + u_o + \hat{C}_o d_L(x_L). \quad (18)$$

If we use the fact that $x = x_1 = \hat{B}_L^{-1}(x_L - u_L)$ and transform the Eulerian variable according to $r \rightarrow r' = \hat{C}_o^{-1}(r - u_o) + \hat{B}_o \hat{B}_L^{-1} u_L$, the above equation can be cast into the form

$$r' = x' + s'(x'), \quad (19a)$$

where $x' \equiv x_L$ and

$$s'(x') = d_L(x') + \hat{S}_L' x', \quad \hat{S}_L' = \hat{C}_o^{-1} \hat{B}_o \hat{B}_L^{-1} - \hat{I}. \quad (19b)$$

Although there is only shear on each lens screen, the matrix \hat{S}_L' is in general a combination of shear and convergence (i.e., it is symmetric but not traceless). Thus, equation (19a) is formally equivalent to the single-plane lens equation for the point-mass lens plus shear and smooth surface density (cf. eq. [15] of Paper I for the point-mass plus shear lens). This is a specific example of the “nonlinear telescope” (or generalized quadrupole lens) discussed by Kovner (1987; see also Schneider et al. 1992).

We are interested in the case in which the shear perturbations on all the lens screens are weak. To first order in \hat{S}_i ,

the expressions for $\hat{\mathbf{C}}_o$, $\hat{\mathbf{B}}_j$, and $\hat{\mathbf{S}}_L$ are

$$\hat{\mathbf{C}}_o \approx \hat{\mathbf{I}} + \sum_{i=L+1}^N \beta_{Li} \hat{\mathbf{S}}_i, \quad \hat{\mathbf{B}}_j \approx \hat{\mathbf{I}} + \sum_{i=1}^{j-1} \beta_{ij} \hat{\mathbf{S}}_i, \quad (20a)$$

$$\hat{\mathbf{S}}_L \approx \sum_{i=1}^L \left(\frac{\chi_{si} \chi_{Lo}}{\chi_{sL} \chi_{io}} \right) \hat{\mathbf{S}}_i + \sum_{i=L+1}^N \left(\frac{\chi_{sL} \chi_{io}}{\chi_{si} \chi_{Lo}} \right) \hat{\mathbf{S}}_i. \quad (20b)$$

Hence $\hat{\mathbf{S}}_L$ is reduced to a shear matrix: $\hat{\mathbf{S}}_L \approx S'(\chi_{Lo}) \hat{\mathbf{T}}(\phi'_L)$, where $S'(\chi_{Lo})$ is the magnitude of the “effective” shear and

$$\hat{\mathbf{T}}(\phi'_L) = \begin{pmatrix} \cos 2\phi'_L & \sin 2\phi'_L \\ \sin 2\phi'_L & -\cos 2\phi'_L \end{pmatrix}. \quad (21)$$

Then equation (19a) reduces to the single-plane lens equation for the point-mass plus weak-shear lens (eq. [15] of Paper I).

In §§ 3.1–3.2 of Paper I, we studied in detail the properties of single-plane lensing by the point-mass plus weak-shear lens. The results are applicable to the mapping from \mathbf{x}' to \mathbf{r}' (eq. [19a]). We can then infer the properties of the lens mapping from \mathbf{x} to \mathbf{r} (eq. [18]) by taking into account the effects of the transformations $\mathbf{x} \rightarrow \mathbf{x}'$ and $\mathbf{r} \rightarrow \mathbf{r}'$. First, it is clear that, to first order in $\hat{\mathbf{S}}_i$, both transformations are a combination of translation and shear distortion, and are one to one. Second, since the deformation tensor

$$\hat{\mathbf{D}} \equiv \frac{\partial \mathbf{r}}{\partial \mathbf{x}} = \left(\frac{\partial \mathbf{r}}{\partial \mathbf{r}'} \right) \left(\frac{\partial \mathbf{r}'}{\partial \mathbf{x}'} \right) \left(\frac{\partial \mathbf{x}'}{\partial \mathbf{x}} \right) = \hat{\mathbf{C}}_o \left(\frac{\partial \mathbf{r}'}{\partial \mathbf{x}'} \right) \hat{\mathbf{B}}_L, \quad (22)$$

there is a simple correspondence between the caustics (and the critical curves) of the mappings in equations (18) and (19a). In addition, because the determinants $|\hat{\mathbf{C}}_o|$ and $|\hat{\mathbf{B}}_L|$ are $1 + O(S'^2)$, the magnification $|\hat{\mathbf{D}}|^{-1}$ at a point \mathbf{r} is, to first order in $S'(\chi_{Lo})$, identical to the “magnification” $|\partial \mathbf{r}' / \partial \mathbf{x}'|^{-1}$ at the corresponding point \mathbf{r}' . Similarly, the correction factors for the differential cross section are $1 + O(S'^2)$. All the corrections that we have just considered are of the same order as the terms already ignored in the weak-shear analysis in Paper I. Therefore, the effects of the transformations are negligible, and the properties derived in §§ 3.1–3.2 of Paper I are also applicable to the lens mapping (eq. [18]). Briefly, for a point-mass lens perturbed by weak shear in three dimensions, the critical line is a slightly flattened ellipse (of size $x_{E,L}$); the caustic has the shape of an astroid with the four cusp catastrophes [at a distance $2x_{E,L} S'(\chi_{Lo})$ from the center of the astroid] connected to each other by four fold catastrophes (see Fig. 2 of Paper I); the differential cross section has the scaling property

$$\sigma[A | S'(\chi_{Lo})] = \frac{2\pi x_{E,L}^2}{(A^2 - 1)^{3/2}} \varphi[AS'(\chi_{Lo})] \quad (23)$$

(see eq. [23] of Paper I), where the normalized differential cross section $\varphi(AS')$ depends on A and $S'(\chi_{Lo})$ only through the combination AS' , and $\varphi(AS')$ (see Fig. 3 of Paper I) shows strong caustic-induced features at the critical values $A_1 = 2/3\sqrt{3} S'$ and $A_2 = 1/S'$.

As mentioned in § 2, when we consider the situation in which a significant fraction of the dark matter in the universe is in the form of cosmologically distributed compact objects, we should compensate the randomly distributed point masses on each lens plane by a negative smooth surface mass density. The derivation in this section can be

generalized to this case if we replace $\hat{\mathbf{S}}_i$ in all the equations (except eq. [12b]) by $\hat{\mathbf{S}}_i + \pi n_i x_{E,i}^2 \hat{\mathbf{I}}$. The results remain valid, but the magnification A should be interpreted as the magnification with respect to an “empty beam” (i.e., a light beam that is not affected by the point masses).³

4.2. Three-dimensional Superposition of Cross Sections with Distributed Shear

As discussed above, in the case of low optical depth microlensing by a three-dimensional distribution of point masses, we can neglect the features associated with the secondary caustics when we consider the macroimage magnification distribution $P(A)$ at $A \gtrsim 2$. Therefore, as in the two-dimensional case (see § 3.3 of Paper I), $P(A)$ at $A \gtrsim 2$ can be approximated as a superposition of the cross sections of the individual point-mass lenses, with the shear perturbation due to the other point masses varying from lens to lens.

Let us assume that the point masses are distributed randomly on N lens planes, each with projected (onto the observer plane) surface number density n_i . Then $P(A)$ can be written as

$$P(A) = n \sum_{L=1}^N p(\chi_{Lo}) \int_0^\infty dS' p(S' | \chi_{Lo}) \sigma(A | S'), \quad (24)$$

where $\sigma(A | S')$ is the cross section given in equation (23), $p(S' | \chi_{Lo})$ is the probability distribution of the effective shear $S'(\chi_{Lo})$ for a dominant lens at χ_{Lo} , $p(\chi_{Lo})$ is the probability that the dominant lens is located on the L th screen, and $n = \sum_{i=1}^N n_i$ is the total projected surface number density. Since $p(\chi_{Lo})$ is simply

$$p(\chi_{Lo}) = n_L/n, \quad (25)$$

we have

$$P(A) = \sum_{L=1}^N P(A | \chi_{Lo}), \quad (26)$$

where

$$P(A | \chi_{Lo}) \equiv n_L \int_0^\infty dS' p(S' | \chi_{Lo}) \sigma(A | S'). \quad (27)$$

The function $P(A | \chi_{Lo})$ has the same structure as $P(A)$ in the two-dimensional case (eq. [29] of Paper I), and it is the contribution to the macroimage magnification distribution by the lenses on the L th lens screen as the dominant lenses.

The effective shear $S'(\chi_{Lo})$ that enters into the cross section $\sigma(A | S')$ is a weighted superposition of the shear induced by all except the dominant lens (eq. [20b]). In the Appendix, we show that

$$p(S' | \chi_{Lo}) = \frac{\tau'(\chi_{Lo}) S'}{[\tau'^2(\chi_{Lo}) + S'^2]^{3/2}}, \quad (28)$$

³ For an empty beam, the lens equation is $\mathbf{x}_j = \mathbf{x}_1 + \sum_{i=1}^{j-1} \beta_{ij} \pi n_i x_{E,i}^2 \mathbf{x}_i$. Thus the average magnification with respect to an empty beam is $\bar{A} = |\hat{\mathbf{D}}|$, where the deformation tensor $\hat{\mathbf{D}} \equiv \partial \mathbf{r} / \partial \mathbf{x} = \hat{\mathbf{I}} + \sum_{i=1}^N \pi n_i x_{E,i}^2 \partial \mathbf{x}_i / \partial \mathbf{x}_1$ and $\partial \mathbf{x}_j / \partial \mathbf{x}_1 = \hat{\mathbf{I}} + \sum_{i=1}^{j-1} \beta_{ij} \pi n_i x_{E,i}^2 \partial \mathbf{x}_i / \partial \mathbf{x}_1$. The average magnification \bar{A} is not a simple analytic function of the optical depth $\tau (= \sum_i \pi n_i x_{E,i}^2)$, but $\bar{A} \approx 1 + 2\tau$ in the limit $\tau \ll 1$.

where

$$\tau'(\chi_{Lo}) = \sum_{i=1}^L \left(\frac{\chi_{si} \chi_{Lo}}{\chi_{sL} \chi_{io}} \right) \pi n_i x_{E,i}^2 + \sum_{i=L+1}^N \left(\frac{\chi_{sL} \chi_{io}}{\chi_{si} \chi_{Lo}} \right) \pi n_i x_{E,i}^2 \quad (29)$$

is the “effective” optical depth at χ_{Lo} . [Note that the effective optical depth $\tau'(\chi_{Lo})$ is smaller than the (usual) optical depth $\tau = \sum_{i=1}^N \pi n_i x_{E,i}^2$, because the extra factors $\chi_{si} \chi_{Lo} / \chi_{sL} \chi_{io}$ (for $i < L$) and $\chi_{sL} \chi_{io} / \chi_{si} \chi_{Lo}$ (for $i > L$) are less than unity.] Substituting equations (23) and (28) into equation (27), we find that $P(A|\chi_{Lo})$ is similar to $P(A)$ for a single lens plane:

$$P(A|\chi_{Lo}) = \frac{2\pi n_L x_{E,L}^2}{(A^2 - 1)^{3/2}} f_1[A\tau'(\chi_{Lo})] \quad (30)$$

(cf. eq. [31] of Paper I), where $f_1(A\tau) = \int_0^\infty dy \phi(A\tau y) y / (1 + y^2)^{3/2}$ is the function introduced in § 3.3 of Paper I to describe the caustic-induced feature in $P(A)$ in the case of a single lens plane (see Fig. 4 of Paper I and also Fig. 12 of this paper). Thus $P(A|\chi_{Lo})$ exhibits the same caustic-induced bump (with a maximum enhancement of 20% at $A \approx 2/\tau$) and the same scaling property (with f_1 being a function of the combination $A\tau$) as $P(A)$ in the single lens plane case.

There is, however, a significant difference between the two- and the three-dimensional cases. To obtain the macroimage magnification distribution in the three-dimensional case, we must sum $P(A|\chi_{Lo})$ over all the lens planes (eq. [26]):

$$P(A) = \sum_{L=1}^N \frac{2\pi n_L x_{E,L}^2}{(A^2 - 1)^{3/2}} f_1[A\tau'(\chi_{Lo})] \\ = \frac{2\tau}{(A^2 - 1)^{3/2}} f_N(A; \tau), \quad (31)$$

where

$$f_N(A; \tau) \equiv \sum_{L=1}^N \left(\frac{\pi n_L x_{E,L}^2}{\tau} \right) f_1 \left[A\tau \frac{\tau'(\chi_{Lo})}{\tau} \right] \quad (32)$$

and $\tau = \pi \sum_{L=1}^N n_L x_{E,L}^2$ is the (usual) optical depth. Although we denote the caustic-induced feature in the N -plane case as $f_N(A; \tau)$ for simplicity, it should be clear from equation (32) that $f_N(A; \tau)$ depends on the location and the surface density of the lens planes in a nontrivial manner and does not have any simple scaling properties (when $N > 1$). Note also that the differences between $f_1(A\tau)$ and $f_N(A; \tau)$ are due to the differences between the optical depths τ and $\tau'(\chi_{Lo})$.

To proceed further, we need to assume a model for the distribution of the point-mass lenses. As in most previous studies (see references cited in § 1), we consider a lens distribution with *constant* comoving mass density ρ_l . We divide the volume between the source and the observer into N shells of equal comoving thickness ($\Delta\chi = \chi_{so}/N$) and place the point masses in each shell on a lens plane at the middle of the shell. In Figure 12, we plot the numerically evaluated $f_N(A; \tau)$ for $N = 1, 2, 4, 8$, and 16, and for source redshifts $z_s \ll 1$ and $z_s = 2$. It is clear that f_N has converged by $N = 16$. This agrees with the conclusion from a study of lensing by smoothly variable mass distribution that a fully three-dimensional mass distribution is well approximated by as few as eight or 16 screens (Lee & Paczyński 1990). It is

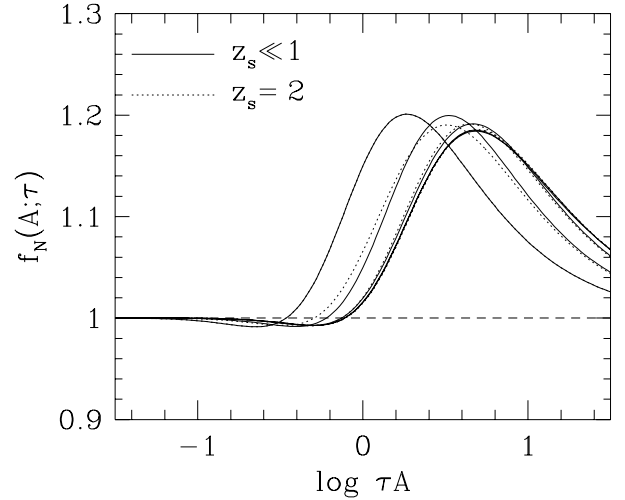


FIG. 12.—The function $f_N(A; \tau)$ (eq. [32]) that describes the caustic-induced feature in the macroimage magnification distribution, $P(A)$, at low optical depth τ . The solid (dashed) lines, from left to right, show f_N for $N = 1, 2, 4, 8$, and 16 and for source redshift $z_s \ll 1$ ($z_s = 2$). A lens distribution with constant comoving mass density is assumed (see § 4.2).

also clear that $f_\infty (\equiv \lim_{N \rightarrow \infty} f_N)$ is very insensitive to the source redshift, at least for $z_s \lesssim 2$.

In the limit $N \rightarrow \infty$, the summations in the expressions for τ , $\tau'(\chi_{Lo})$, and $f_N(A; \tau)$ are replaced by integrals:

$$\tau = 4\pi G \rho_l a_0^3 \int_0^{\chi_{so}} d\chi \frac{\chi(\chi_{so} - \chi)}{a(\chi)\chi_{so}}; \quad (33a)$$

$$\tau'(\chi_{Lo}) = 4\pi G \rho_l a_0^3 \left[\int_0^{\chi_{sL}} d\chi \frac{\chi_{Lo} \chi^2}{a(\chi)\chi_{so}\chi_{sL}} + \int_{\chi_{sL}}^{\chi_{so}} d\chi \frac{\chi_{sL}(\chi_{so} - \chi)^2}{a(\chi)\chi_{so}\chi_{Lo}} \right]; \quad (33b)$$

$$f_\infty(A; \tau) = \frac{4\pi G \rho_l a_0^3}{\tau} \int_0^{\chi_{so}} d\chi \frac{\chi(\chi_{so} - \chi)}{a(\chi)\chi_{so}} f_1 \left(A\tau \frac{\tau'}{\tau} \right). \quad (33c)$$

Equations (33a)–(33b) can be evaluated analytically. They are particularly simple in the limit $z_s \ll 1$ [i.e., in the limit $a(\chi_{so}) \approx a_0$]:

$$\tau \approx \frac{2\pi}{3} G \rho_l a_0^2 \chi_{so}^2; \quad (34a)$$

$$\tau'(\chi_{Lo}) \approx \frac{4\pi}{3} G \rho_l a_0^2 \chi_{sL} \chi_{Lo}; \quad (34b)$$

$$f_\infty(A; \tau) \approx 6 \int_0^{\chi_{so}} d\chi \frac{\chi(\chi_{so} - \chi)}{\chi_{so}^3} f_1 \left[A\tau \frac{2\chi(\chi_{so} - \chi)}{\chi_{so}^2} \right]. \quad (34c)$$

Thus the contribution to f_∞ is dominated by the lens planes at $\chi_{Lo} \approx \chi_{so}/2$, with $\tau'/\tau \lesssim \frac{1}{2}$. This is consistent with the numerical results shown in Figure 12. The most significant change from f_1 to f_∞ is the shift in the location of the bump from $A\tau \approx 2$ to $A\tau \approx 5$. Otherwise, the peak value ($\approx 18\%$ enhancement) and the width of f_∞ are only slightly smaller and wider.

4.3. Comparison with Numerical Simulations

Several authors (Refsdal 1970; Schneider & Weiss 1988a, 1988b; Rauch 1991) have used numerical simulations to calculate the macroimage magnification distribution, $P(A)$, produced by a three-dimensional distribution of point

masses. In the most recent study by Rauch, distributions with high resolution in A were obtained from Monte Carlo simulations for three cases with $\sigma = 0.01, 0.1$, and 0.2 . The “equivalent σ -value” is defined in terms of the average magnification \bar{A} (with respect to an empty beam) on the observer plane: $\bar{A} = (1 - \sigma)^{-2}$, i.e., σ is the optical depth τ of a two-dimensional lens distribution with the same \bar{A} . For a three-dimensional lens distribution, \bar{A} is not a simple analytic function of τ (see footnote 3), and σ and τ are not identical in general, but $\bar{A} \approx 1 + 2\tau \approx 1 + 2\sigma$ in the limit $\tau \ll 1$.

We wish to compare the semianalytic $P(A)$ derived in § 4.2 with the distributions obtained by Rauch. (We shall focus on Rauch’s results for an Einstein–de Sitter cosmological background, but he also found that the distributions for the same σ but different background cosmology are nearly identical.) Since our derivation assumes low optical depth, the best case for comparison should be the $\sigma = 0.01$ case. Unfortunately, even with 5×10^5 simulations, the Monte Carlo simulations only provide useful information about $P(A)$ for $A < 50$ (see Fig. 2 in Rauch 1991). This is not sufficient for detecting the caustic-induced feature, because significant deviation from $P(A) = 2\tau/(A^2 - 1)^{3/2}$ is not expected for $A \lesssim 1/\tau$ (≈ 100 for $\tau \approx \sigma = 0.01$) (see f_∞ in Fig. 12). We shall not show the comparison for this case; we simply note that the numerically obtained $P(A)$ (for $A < 50$) agrees with the low optical depth semianalytic result, with or without the caustic-induced feature.

In Figure 13, we show the distributions obtained by Rauch for $\sigma = 0.1$ and 0.2 (histograms). The data are those shown in Figures 3 and 4 of Rauch (1991), but they are plotted in the form $(A^2 - 1)^{3/2}P(A)$, and we have increased the bin sizes at large A to reduce statistical fluctuations. As Rauch et al. (1992) pointed out, the distributions in the three-dimensional case do not show the prominent bump at $A \gtrsim 2.5$ that was found in the planar case. However, the distributions are not featureless. This can be seen most clearly in the $\sigma = 0.2$ case (note, e.g., the inflection point at $\log A \approx 0.6$).

In a plot of $(A^2 - 1)^{3/2}P(A)$, the low optical depth distribution without the caustic-induced feature is a horizontal

line of amplitude $K = 2\tau$, while the semianalytic distribution with the caustic-induced feature is $Kf_\infty(A; \tau)$ (eq. [31]; recall that f_∞ is insensitive to the source redshift). For $\sigma = 0.1$ and 0.2 , two corrections to the low optical depth semianalytic results are necessary when we compare them with the numerical ones. First, it is not sufficient to assume that $\tau = \sigma$. For these particular models, $\sigma = 0.1$ and 0.2 correspond to $\tau = 0.108$ and 0.233 , respectively. Second, the normalization K can differ significantly from the low optical depth result 2τ . In § 5.1 of Paper I, we discussed the renormalization of $P(A)$ due to the net convergence of light rays and multiple streaming for the single lens plane case. From an analytic result for $P(A)$ in the very high magnification ($A \gg 1/\tau$) limit, which is exact even for finite optical depth τ (see also Schneider 1987), we adopted the normalization

$$K = 2\tau \frac{\bar{A}}{(1 + \tau^2)^{3/2}}. \quad (35)$$

[For $\tau \ll 1$, $\bar{A} \approx 1 + 2\tau$ and $(1 + \tau^2)^{-3/2} \approx 1 - 3\tau^2/2$.] The analysis that led to equation (35) cannot be easily generalized to the three-dimensional case (it would require the statistical properties of the matrix $\hat{\mathbf{B}}_o$, which depends on the shear matrices $\hat{\mathbf{S}}_i$ nonlinearly; see eq. [14]), and an equivalent expression for K for a three-dimensional lens distribution is not known. Nevertheless, in the range of τ of interest here (i.e., for $\tau \lesssim 0.25$), it is likely that equation (35) is a good approximation for K in the three-dimensional case. In equation (35), the dominant correction to the normalization 2τ is the factor \bar{A} . [The correction due to the factor $(1 + \tau^2)^{-3/2}$ is second order in τ and less than 10% for $\tau \lesssim 0.25$.] The factor \bar{A} arises from converting a probability distribution in Lagrangian space to a distribution in Eulerian space (see § 5.1 of Paper I). The conversion (and hence the factor \bar{A}) should remain in any generalization of the analysis to the three-dimensional case. Furthermore, as in the planar case (see § 5.1 of Paper I), we can derive the factor \bar{A} by using a different argument: In § 4.2, we assumed that the surface density of the astroid-shaped caustics on the observer plane is the same as the projected surface density of point masses n (see eq. [24]); there is, however, a net convergence of the light rays by the overall lens distribution that increases the density of astroids by a factor of \bar{A} and introduces an additional factor of \bar{A} in the normalization of $P(A)$ in equation (31). Therefore, we shall adopt equation (35) for the normalization K in the three-dimensional case.

In Figure 13, we plot K (dashed lines) and $Kf_\infty(A; \tau)$ (solid lines) for $\sigma = 0.1$ and 0.2 . They should be compared with the numerical results at $A \gtrsim 2$, or $\log A \gtrsim 0.3$ (see § 4.5 for a brief discussion of the deviations at $A \lesssim 2$). As can be seen, the adopted normalization K is in good agreement with the amplitudes of the numerical results. In addition, the numerical results show deviations from the horizontal dashed lines that are similar in shape to the semianalytic caustic-induced feature f_∞ (note, e.g., that the inflection point in the numerical result for $\sigma = 0.2$ coincides with the location $A \approx 1/\tau$, where f_∞ starts to deviate significantly from unity). In the $\sigma = 0.1$ case, there is little, if any, difference between the numerical and semianalytic results; the only possibly statistically significant deviation is that the numerical distribution may be higher near $\log A \approx 1$. In the $\sigma = 0.2$ case, the difference between the numerical and semi-

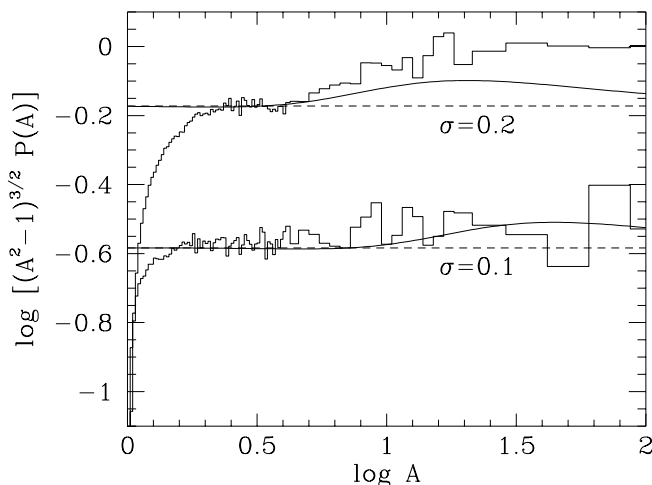


FIG. 13.—Comparison of the semianalytic macroimage magnification distribution $P(A) = Kf_\infty(A; \tau)/(A^2 - 1)^{3/2}$ (solid lines) with the Monte Carlo results of Rauch (1991; histograms) for $\sigma = 0.1$ and 0.2 (or optical depths $\tau = 0.108$ and 0.233). We adopt eq. (35) for the normalization K (dashed lines).

analytic results is more pronounced, with the numerical distribution slightly higher than the semianalytic distribution over the range $0.7 < \log A < 2$. Note, however, that the number of events in the histograms at $\log A > 1.6$ is small (see the fluctuations among the same bins in the $\sigma = 0.1$ case), and the true distribution may not be as flat as the histograms shown.

4.4. Criterion for Low Optical Depth

The comparison in § 4.3 shows that, in the case of a three-dimensional lens distribution, the function f_∞ , which was derived in the low optical depth limit, provides a reasonably good fit to the caustic-induced feature in $P(A)$ for τ as large as 0.233. This is very different from the two-dimensional case studied in Paper I. For a two-dimensional lens distribution, the caustic-induced feature in the numerically obtained $P(A)$ is more prominent than the low optical depth semianalytic feature f_1 for τ as small as 0.1. This was shown in Figure 6 of Paper I, where we compared the numerical and semianalytic distributions for $\tau (= \sigma) = 0.1$ and 0.2 in a plot of $(A^2 - 1)^{3/2} P(A)$. The numerical distributions show a clear minimum at $A \approx 2.5$ and are significantly higher than the semianalytic results in the range $0.5 \lesssim \log A \lesssim 1$.

For both the two- and three-dimensional lens distributions, the low optical depth analysis assumes that the point-mass lenses are well separated in Lagrangian space (i.e., in projection). Then the deflection near each point mass is due to that point mass and the shear perturbation from the other lenses, and an astroid-shaped (primary) caustic is associated with each point mass. The low optical depth analysis is not valid if the lens density is high enough that a significant fraction of the lenses have close neighbor(s), and their caustics are complex structures produced by the collective effect of two (or more) point masses. In § 5.3 of Paper I, we estimated for the two-dimensional case the fraction of point masses whose caustics are not isolated astroids, $P_{na}(\tau)$, by considering a point mass and its nearest neighbor as a two-point-mass lens: $P_{na}(\tau) = 1 - \exp(-8\tau)$. For $\tau = 0.1$, $P_{na} = 0.55$. This explains the relatively strong contribution to $P(A)$ by the collective effect of two (or more) point masses (which results in the enhanced caustic-induced feature at moderate A) for τ as small as 0.1.

To understand the difference between the two- and three-dimensional cases, we need to estimate $P_{na}(\tau)$ for the three-dimensional case. We now extend the method used in Paper I to estimate $P_{na}(\tau)$ to the three-dimensional case. We begin by considering lensing configurations with two point masses on different lens planes. Since our results in § 4.2 and the numerical results of Rauch (1991) show that $P(A)$ is not sensitive to either the source redshift or the background cosmology, we shall simplify the analysis by assuming that $a(\chi_{so}) \approx a_0$. Then the two-point-mass configurations of interest are identical to those studied in § 3.1 and are specified by two parameters: the dimensionless distance β_{ij} between the lens planes and the dimensionless Lagrangian separation d between the lenses [the actual Lagrangian separation is $(x_{E,i}^2 + x_{E,j}^2)^{1/2} d$; see eq. (7)]. Note that we have changed the notation slightly and that the point masses are on lens planes i and j instead of lens planes 1 and 2. As we saw in § 3.1, the topology of the caustics (and the critical curves) changes with decreasing d from type A to type F. The only topology with two astroid-shaped primary caustics is type A; the other topology types are produced by the

strong effect of both point masses (see Fig. 5). In Figure 14, we plot the separation d_{AB} at which the topology changes from type A to type B as a function of β_{ij} . (The data were obtained using the numerical code that generated the caustics and critical curves shown in Figs. 2–9.) The separation d_{AB} decreases with increasing β_{ij} . In the limit $\beta_{ij} = 0$, the two point masses are on the same plane, and we have $d_{AB} = 2$ (Schneider & Weiss 1986). In the limit $\beta_{ij} \rightarrow 1$ (i.e., in the limit $i \rightarrow "s"$ or $j \rightarrow "o"$; see eq. [2]), $d_{AB} \rightarrow 0$; this is due to the focusing of the light rays by the point mass on lens plane i and the fact that $x_{E,j}/x_{E,i} \rightarrow 0$.

Let us consider first a simple extension of the method used in Paper I to estimate $P_{na}(\tau)$. It is convenient to consider the projected distribution (i.e., the distribution in Lagrangian space) of the point-mass lenses. If we select randomly one of the point masses, the probability that the point mass is on lens plane i is n_i/n , where $n = \sum_{i=1}^N n_i$ is the total projected surface number density of point masses. This point mass has an absolute nearest neighbor in Lagrangian space. Since the point masses are distributed randomly, the probability that the absolute nearest neighbor is on lens plane j and at a Lagrangian distance less than r is $(n_j/n)[1 - \exp(-\pi n r^2)]$. If we ignore the deflection due the other lenses and consider the point mass and its nearest neighbor as a two-point-mass lens, the discussion in the previous paragraph indicates that the primary caustic associated with the point mass is not an isolated astroid if $r < (x_{E,i}^2 + x_{E,j}^2)^{1/2} d_{AB}(\beta_{ij})$. Therefore, an estimate of the fraction of point masses whose caustics are not isolated astroids is

$$P'_{na,N}(\tau) = \sum_{i,j=1}^N \frac{n_i n_j}{n^2} \{1 - \exp[-\pi n (x_{E,i}^2 + x_{E,j}^2) d_{AB}^2(\beta_{ij})]\} . \quad (36)$$

In the three-dimensional case, since the (Lagrangian) Einstein radius $x_{E,L}$ increases from 0 to ∞ as χ_{Lo} increases (see eq. [6]), it is possible, e.g., for the primary caustic (and critical curve) of a point mass to merge with that of its second nearest neighbor (from plane k), but not with that of its absolute nearest neighbor (from plane j), if $x_{E,k} \gg x_{E,j}$. Thus the function $P'_{na,N}(\tau)$, which takes into account the absolute nearest neighbor only, probably underestimates

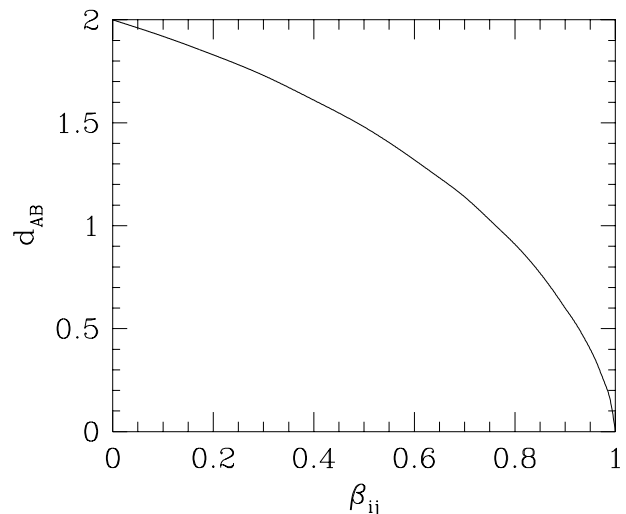


FIG. 14.—Lagrangian separation d_{AB} at which the critical curve (and caustic) topology of the two-point-mass lens changes from type A to type B as a function of β_{ij} .

the fraction of point masses whose caustics are not isolated astroids. We can derive a better estimate by taking into account the nearest neighbors from all the lens planes. For a randomly selected point mass (on lens plane i with probability n_i/n), the probability that the nearest neighbor from lens plane j is at Lagrangian distance greater than r is $\exp(-\pi n_j r^2)$. If we ignore the deflection due to the other lenses and consider the point mass and its nearest neighbor from lens plane j as a two-point-mass lens, the two-point-mass lens produces two astroid-shaped primary caustics if $r > (x_{E,i}^2 + x_{E,j}^2)^{1/2} d_{AB}(\beta_{ij})$. Thus the probability that the primary caustic associated with the point mass is an isolated astroid is $\prod_{j=1}^N \exp[-\pi n_j (x_{E,i}^2 + x_{E,j}^2) d_{AB}^2(\beta_{ij})]$. Therefore, a better estimate of the fraction of point masses whose caustics are not isolated astroids is

$$P_{na,N}(\tau) = \sum_{i=1}^N \frac{n_i}{n} \times \left\{ 1 - \exp \left[-\pi \sum_{j=1}^N n_j (x_{E,i}^2 + x_{E,j}^2) d_{AB}^2(\beta_{ij}) \right] \right\}. \quad (37)$$

As with $f_N(A; \tau)$, although $P'_{na,N}$ and $P_{na,N}$ are denoted as functions of τ , they do depend on the location and the surface density of the lens planes. For $N = 1$, i.e., for a single lens plane, both $P_{na,N}(\tau)$ and $P'_{na,N}(\tau)$ reduce correctly to $P_{na}(\tau) = 1 - \exp(-8\tau)$. In the limit $\tau \ll 1$,

$$P_{na,N}(\tau) \approx P'_{na,N}(\tau) \approx \tau \sum_{i,j} \left(\frac{n_i n_j}{n^2} \right) \frac{\pi n (x_{E,i}^2 + x_{E,j}^2)}{\tau} d_{AB}^2(\beta_{ij}). \quad (38)$$

In Figure 15, we show $P'_{na,N}(\tau)$ for $N = 1, 2, 4, 8$, and ∞ (dashed lines) and $P_{na,\infty}(\tau)$ (solid line), using the constant comoving density model adopted in § 4.2. Both $P'_{na,N}$ and $P_{na,N}$ have converged by $N \approx 16$. The difference between $P'_{na,\infty}$ and $P_{na,\infty}$ is small for $\tau \lesssim 0.1$, but it increases to 0.10 at $\tau = 0.5$.

It is clear from Figure 15 that $P_{na,\infty}(\tau)$ is significantly smaller than $P_{na}(\tau)$ (Fig. 15, uppermost dashed curve). In the limit $\tau \ll 1$, $P_{na,\infty}(\tau) \approx P'_{na,\infty}(\tau) \approx 2.5\tau$ while $P_{na}(\tau) \approx 8\tau$

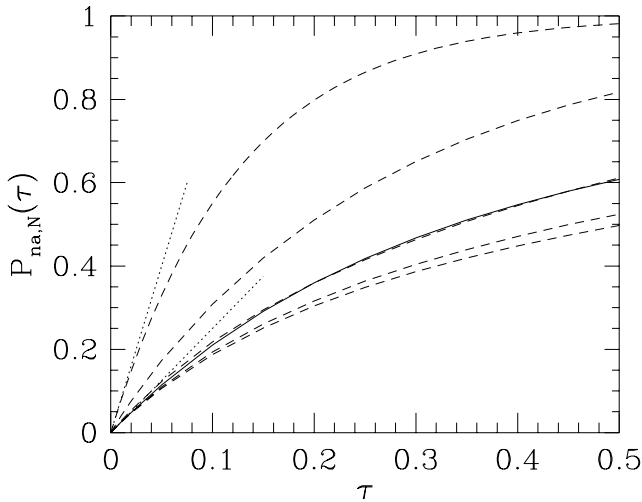


FIG. 15.—Fraction of point masses whose caustics are not isolated astroids as a function of the optical depth τ . The dashed lines, from top to bottom, are $P'_{na,N}$ (eq. [36]) for $N = 1, 2, 4, 8$, and ∞ , and the solid line is $P_{na,\infty}$ (eq. [37]). The dotted lines show the asymptotes $P_{na,\infty} \approx P'_{na,\infty} \approx 2.5\tau$ and $P_{na} \approx 8\tau$ for $\tau \ll 1$. A lens distribution with constant comoving mass density is assumed (see § 4.2).

(dotted lines). For $\tau = 0.1$, $P_{na,\infty} = 0.20$ and $P_{na} = 0.55$; even for $\tau = 0.233$, $P_{na,\infty} = 0.40$ only. Thus, in the three-dimensional case, both the fraction of point masses whose (primary) caustics are not isolated astroids and the contribution to $P(A)$ by configurations of two (or more) point masses are much smaller. This explains why the low optical depth semianalytic feature f_∞ provides a reasonably good fit to the caustic-induced feature in $P(A)$ for τ as large as 0.233. At sufficiently large τ (> 0.35), $P_{na,\infty} > 0.5$ and $P(A)$ should deviate significantly from the semianalytic result.

4.5. Modification of $P(A)$ at Low Magnification

Finally, we discuss briefly the deviations of $P(A)$ from the semianalytic distribution $Kf_\infty/(A^2 - 1)^{3/2}$ at low magnification, $A \lesssim 2$ (see Fig. 13). As in the planar case, the superposition of the cross sections of individual lenses that results in the caustic-induced feature f_∞ is only valid for the magnifications seen by the observers close to one of the astroid-shaped primary caustics. The semianalytic distribution also requires modification at low magnification, as it diverges as $(A - 1)^{-3/2}$ at $A = 1$ and is not normalizable. In the planar case, an observer not particularly well aligned with any single lens sees a primary image close to the unperturbed position of the source and a large number of faint secondary images (one close to each lens) produced by strongly deflected rays. In Paper I, we took into account the correlations between the magnifications of the primary and the secondary images and derived the modification of $P(A)$ at low magnification ($A - 1 \ll 1$). We have not attempted a similar calculation in the three-dimensional case, because the problem is significantly more complicated. First, for an observer that is not particularly close to either a primary or a secondary caustic, there are now $\sim 2^{N*}$ secondary images (where N^* is the number of lenses) because a light ray can reach the observer after being strongly deflected by one or more lenses. Although the secondary images that have been strongly deflected by more than one lens are typically much fainter than those that have been strongly deflected by only one lens, they are far more numerous and we may have to account for them. A more serious problem is the presence of weak caustic-induced features at $A \lesssim 2$ that are associated with the secondary caustics (see § 3). Unlike the features associated with the primary caustics at high magnification, there are no simple semianalytic descriptions of the features associated with the secondary caustics. The regime in which the superposition calculation is valid is also affected by the presence of secondary caustics. In the three-dimensional case, the superposition calculation is probably only valid for $A \gtrsim 2$; in the planar case, the superposition of cross sections is valid for $A - 1 \gg \tau^2$.

5. SUMMARY

In this paper and in Paper I, we have sought to develop a systematic theory of gravitational microlensing in the low optical depth limit. We focused on microlensing by a planar distribution of point masses in Paper I. In this paper, we have studied gravitational microlensing by a three-dimensional distribution of point masses, focusing on the nature of the critical curves, the caustics, the illumination pattern, and especially the macroimage magnification distribution $P(A)$. In the process, we have explained many of the differences between two- and three-dimensional microlensing that have been seen in previous numerical simulations.

In § 3, we studied the lensing properties of three-dimensional lens distributions by considering in detail multiplane configurations with two, three, and four point masses. The lensing properties of a three-dimensional lens distribution are fundamentally different from those of a planar distribution, in that a light ray could have arrived in the vicinity of a lens either having suffered only weak deflections along the way from the source or after having been strongly deflected one or more times by the intervening lenses. The latter situation cannot arise in a purely planar distribution of lenses, and it gives rise to secondary caustics and critical lines that have no analogs in the planar case. In addition, in the case of more than two point masses, the caustic topology is no longer simply related to the critical curve topology, because caustics corresponding to different critical lines may overlap each other.

For N_* point masses that are widely separated in Lagrangian space (i.e., in projection), there are $\sim N_*$ primary critical curves (i.e., critical curves that have not suffered any strong deflections) and $\sim 2N_* - 1$ critical curves in total. Features in the “normalized” differential cross section, $\varphi(A)$, that are associated with the secondary caustics are relatively weak and at $A \lesssim 2$. Significant features occurring at moderate to high magnifications ($A \gtrsim 2$) are invariably associated with the primary caustics.

In § 4, we derived a semianalytic expression for the caustic-induced feature at the high-magnification ($A \sim 1/\tau$) end of $P(A)$ for a low optical depth lens distribution. In the low optical depth limit, we showed that the multiplane lens equation near a point mass is formally equivalent to the single-plane equation of a point mass perturbed by shear. Consequently, the (primary) caustic has the familiar astroid shape, and the differential cross section exhibits the same scaling behavior found in Paper I (i.e., φ depends on magnification A and the effective shear S' through the combination AS'). By modeling the illumination pattern as a superposition of the patterns due to individual “point-mass

plus weak-shear” lenses, we found that the caustic-induced feature in the macroimage magnification distribution $P(A)$ can be written as a weighted sum of the semianalytic feature derived in Paper I for a planar lens distribution (eq. [32]). The resulting semianalytic caustic-induced feature is similar to the feature in the planar case, but it is shifted to higher magnification.

At $A \gtrsim 2$, our semianalytic $P(A)$ agrees remarkably well with the magnification distribution obtained from numerical simulations by Rauch (1991), even for optical depth as high as $\tau \approx 0.2$. This is very different from the two-dimensional case studied in Paper I. In the two-dimensional case, we have found that the caustic-induced feature in $P(A)$ tends to be more pronounced than the low optical depth result, even for optical depth as low as $\tau \approx 0.1$. We argued that this particular difference between two- and three-dimensional microlensing is due to the fact that, for a given value of optical depth, the fraction of point masses whose (primary) caustics are not simple astroids is significantly higher in the planar case than in the three-dimensional case. Finally, we discussed briefly the deviations of the numerical $P(A)$ from the semianalytic distribution at $A \lesssim 2$. In the three-dimensional case, a simple criterion for the low optical depth analysis to be valid is $P_{\text{na},\infty} \approx P'_{\text{na},\infty} \approx 2.5\tau \ll 1$ or $\tau \ll 0.4$, though the comparison with numerical simulations indicates that the semianalytic distribution is a reasonable fit to $P(A)$ for τ up to 0.2.

We thank K. Rauch for providing us with the results of Rauch (1991). We also thank S. Mao and K. Rauch for helpful discussions. A. B. and L. K. acknowledge the hospitality shown to them at CITA during their visits in 1995. This work was supported in part by NSERC (Canada), the CIAR cosmology program, CITA, the Institute for Astronomy (L. K.), the Dudley Observatory (A. B.), and a CITA National Fellowship (M. H. L.).

APPENDIX

STATISTICS OF SHEAR FOR A LOW OPTICAL DEPTH, THREE-DIMENSIONAL LENS DISTRIBUTION

In this appendix, we evaluate $p(S' | \chi_{Lo})$, the probability distribution of the effective shear $S'(\chi_{Lo})$ at a given χ_{Lo} , due to a low optical depth, three-dimensional distribution of point masses. It is assumed that the point masses are distributed randomly on N lens planes, each with projected (onto the observer plane) surface number density n_i . Specifically, on each lens plane, $N_i = \pi n_i R_i^2$ point masses are distributed randomly within a circle of Lagrangian radius R_i .

At a given χ_{Lo} , the effective shear (in matrix form) is

$$\hat{S}'_L = S'(\chi_{Lo}) \hat{T}(\phi'_L) = \sum_{i=1}^L \left(\frac{\chi_{si} \chi_{Lo}}{\chi_{sL} \chi_{io}} \right) \hat{S}_i + \sum_{i=L+1}^N \left(\frac{\chi_{sL} \chi_{io}}{\chi_{si} \chi_{Lo}} \right) \hat{S}_i \quad (\text{A1})$$

(eq. [20b]), where

$$\hat{S}_i = x_{E,i}^2 \sum_{k=1}^{N_i} \frac{1}{|x_{ik}|^2} \begin{pmatrix} \cos 2\phi_{ik} & \sin 2\phi_{ik} \\ \sin 2\phi_{ik} & -\cos 2\phi_{ik} \end{pmatrix} \quad (\text{A2})$$

(eq. [12b]). It is convenient to represent the two distinct components of the shear matrix \hat{S}_i as a vector:

$$S_i = x_{E,i}^2 \sum_k s_{ik}, \quad (\text{A3})$$

where $s_{ik} = (\cos 2\phi_{ik}/|x_{ik}|^2, \sin 2\phi_{ik}/|x_{ik}|^2)$. Then the effective shear \hat{S}'_L can be written as an appropriately weighted vector superposition:

$$S'(\chi_{Lo}) = \sum_{i=1}^L \left(\frac{\chi_{si} \chi_{Lo}}{\chi_{sL} \chi_{io}} \right) x_{E,i}^2 \sum_k s_{ik} + \sum_{i=L+1}^N \left(\frac{\chi_{sL} \chi_{io}}{\chi_{si} \chi_{Lo}} \right) x_{E,i}^2 \sum_k s_{ik} \equiv \sum_{i=1}^N G_i \sum_k s_{ik}, \quad (\text{A4})$$

where we have defined G_i to simplify the notation.

Since all the s_{ik} are statistically independent and have similar statistical properties, the formal expression for the probability distribution of $S'(\chi_{Lo})$ is

$$p(S' | \chi_{Lo}) = \int \cdots \int \prod_{i=1}^N \prod_k d^2 s_{ik} p(s_{ik}) \delta^2 \left(S' - \sum_{i=1}^N G_i \sum_k s_{ik} \right), \quad (A5)$$

where $\delta^2(s)$ is the two-dimensional delta function. To evaluate equation (A5), it is convenient to express the delta function and $p(s_{ik})$ as Fourier transforms:

$$\delta^2 \left(S' - \sum_{i=1}^N G_i \sum_k s_{ik} \right) = \frac{1}{(2\pi)^2} \int d^2 u \exp \left[-i u \cdot \left(S' - \sum_{i=1}^N G_i \sum_k s_{ik} \right) \right], \quad (A6)$$

$$p(s_{ik}) = \frac{1}{(2\pi)^2} \int d^2 t_{ik} q(t_{ik}) e^{-i t_{ik} \cdot s_{ik}}, \quad (A7)$$

where the characteristic function $q(t_{ik})$ is

$$q(t_{ik}) = 1 - \frac{\pi n_i}{N_i} t_{ik} \quad (A8)$$

(Nityananda & Ostriker 1984). Substituting equations (A6) and (A7) into equation (A5), we can perform the integration with respect to s_{ik} :

$$\frac{1}{(2\pi)^2} \int d^2 s_{ik} e^{-i s_{ik} \cdot (t_{ik} - G_i u)} = \delta^2(t_{ik} - G_i u). \quad (A9)$$

Next, we integrate with respect to t_{ik} , grouping together the N_i integrals associated with the i th screen:

$$\int \cdots \int \prod_{k=1}^{N_i} d^2 t_{ik} q(t_{ik}) \delta^2(t_{ik} - G_i u) = \left(1 - \frac{\pi n_i G_i u}{N_i} \right)^{N_i} \rightarrow e^{-\pi n_i G_i u} \quad (A10)$$

in the limit $N_i \rightarrow \infty$. Hence

$$p(S' | \chi_{Lo}) = \frac{1}{(2\pi)^2} \int d^2 u e^{-\tau' u} e^{-i u \cdot S'}, \quad (A11)$$

where the “effective” optical depth $\tau'(\chi_{Lo})$ is

$$\tau'(\chi_{Lo}) = \pi \sum_i G_i n_i = \sum_{i=1}^L \left(\frac{\chi_{si} \chi_{Lo}}{\chi_{sL} \chi_{io}} \right) \pi n_i x_{E,i}^2 + \sum_{i=L+1}^N \left(\frac{\chi_{sL} \chi_{io}}{\chi_{si} \chi_{Lo}} \right) \pi n_i x_{E,i}^2. \quad (A12)$$

Performing the integration with respect to u in equation (A11), we obtain

$$p(S' | \chi_{Lo}) = \frac{1}{2\pi} \int_0^\infty du u e^{-\tau' u} J_0(S' u) = \frac{1}{2\pi} \frac{\tau'}{(\tau'^2 + S'^2)^{3/2}}. \quad (A13)$$

Since $p(S' | \chi_{Lo})$ depends only on the magnitude of the effective shear $S'(\chi_{Lo})$, it is convenient to consider the probability distribution for the latter:

$$p(S' | \chi_{Lo}) = \frac{\tau'(\chi_{Lo}) S'}{[\tau'^2(\chi_{Lo}) + S'^2]^{3/2}}. \quad (A14)$$

We have expressed the probability distribution explicitly as a conditional probability that depends on the value of χ_{Lo} . It should be noted that $p(S' | \chi_{Lo})$ has the same functional form as the shear distribution due to a planar random distribution of point masses (eq. [30] of Paper I).

REFERENCES

- Alard, C., Mao, S., & Guibert, J. 1995, A&A, 300, L17
 Alcock, C., et al. 1993, Nature, 365, 621
 ———, 1997, ApJ, 486, 697
 Ansari, R., et al. 1996, A&A, 314, 94
 Aubourg, E., et al. 1993, Nature, 365, 623
 Babul, A., & Lee, M. H. 1991, MNRAS, 250, 407
 Bernstein, G. M., Tyson, J. A., & Kochanek, C. S. 1993, AJ, 105, 816
 Blandford, R. D., & Narayan, R. 1986, ApJ, 310, 568
 Canizares, C. R. 1982, ApJ, 263, 508
 Carr, B. J. 1994, ARA&A, 32, 531
 Dahle, H., Maddox, S. J., & Lilje, P. B. 1994, ApJ, 435, L79
 Dalcanton, J. J., Canizares, C. R., Granados, A., Steidel, C. C., & Stocke, J. T. 1994, ApJ, 424, 550
 Erdl, H., & Schneider, P. 1993, A&A, 268, 453 (ES)
 Griest, K. 1991, ApJ, 366, 412
 Jaroszyński, M. 1991, MNRAS, 249, 430
 Jaroszyński, M., Park, C., Paczyński, B., & Gott, J. R. 1990, ApJ, 365, 22
 Kayser, R., Refsdal, S., & Stabell, R. 1986, A&A, 166, 36
 Kochanek, C. S., & Apostolakis, J. 1988, MNRAS, 235, 1073
 Kofman, L., Kaiser, N., Lee, M. H., & Babul, A. 1997, ApJ, 489, 508 (Paper I)
 Kovner, I. 1987, ApJ, 316, 52
 Lawrence, C. R., Neugebauer, G., & Matthews, K. 1993, AJ, 105, 17
 Lee, M. H., & Paczyński, B. 1990, ApJ, 357, 32
 Levine, H. I., & Petters, A. O. 1993, A&A, 272, L17
 Levine, H. I., Petters, A. O., & Wambsganss, J. 1993, J. Math. Phys., 34, 4781
 Mao, S., & Paczyński, B. 1991, ApJ, 374, L37
 Nemiroff, R. J. 1989, ApJ, 341, 579
 Nityananda, R., & Ostriker, J. P. 1984, J. Astrophys. Astron., 5, 235

- Paczynski, B. 1986, *ApJ*, 304, 1
———. 1991, *ApJ*, 371, L63
Pei, Y. C. 1993, *ApJ*, 403, 7
Pelló, R., Miralles, J. M., Le Borgne, J.-F., Picat, J.-P., Soucail, G., & Bruzual, G. 1996, *A&A*, 314, 73
Petters, A. O. 1995a, *J. Math. Phys.*, 36, 4263
———. 1995b, *J. Math. Phys.*, 36, 4276
Petters, A. O., & Wicklin, F. J. 1995, *MNRAS*, 277, 1399
Press, W. H., & Gunn, J. E. 1973, *ApJ*, 185, 397
Rauch, K. P. 1991, *ApJ*, 374, 83
Rauch, K. P., Mao, S., Wambsganss, J., & Paczyński, B. 1992, *ApJ*, 386, 30
Refsdal, S. 1970, *ApJ*, 159, 357
Schneider, P. 1987, *ApJ*, 319, 9
———. 1993, *A&A*, 279, 1
Schneider, P., Ehlers, J., & Falco, E. E. 1992, *Gravitational Lenses* (New York: Springer)
Schneider, P., & Weiss, A. 1986, *A&A*, 164, 237
———. 1988a, *ApJ*, 327, 526
———. 1988b, *ApJ*, 330, 1
Turner, E. L., Ostriker, J. P., & Gott, J. R. 1984, *ApJ*, 284, 1
Udalski, A., Szymański, M., Kałużny, J., Kubiak, M., Krzemiński, W., Mateo, M., Preston, G. W., & Paczyński, B. 1993, *Acta Astron.*, 43, 289
Udalski, A., Szymański, M., Mao, S., Di Stefano, R., Kałużny, J., Kubiak, M., Mateo, M., & Krzemiński, W. 1994a, *ApJ*, 436, L103
Udalski, A., et al. 1994b, *Acta Astron.*, 44, 165
Wambsganss, J., Cen, R., & Ostriker, J. P. 1996, *ApJ*, submitted (astro-ph/9610096)